Implications for atmospheric dynamics derived from global observations of gravity wave momentum flux in stratosphere and mesosphere

M. Ern,[1] P. Preusse,[1] J. C. Gille,[2,3] C. L. Hepplewhite,[4] M. G. Mlynczak,[5] J. M. Russell III,[6] and M. Riese[1]

Received 16 February 2011; revised 21 June 2011; accepted 20 July 2011; published 8 October 2011.

[1] In this work absolute values of gravity wave (GW) momentum flux are derived from global temperature measurements by the satellite instruments High Resolution Dynamics Limb Sounder (HIRDLS) and Sounding of the Atmosphere using Broadband Emission Radiometry (SABER). Momentum fluxes in the stratosphere are derived for both instruments and for SABER in the whole mesosphere. The large-scale atmospheric background state is removed by a two-dimensional Fourier decomposition in longitude and time, covering even planetary-scale waves with periods as short as 1–2 days. Therefore, it is possible to provide global distributions of GW momentum flux from observations for the first time in the mesosphere. Seasonal as well as longer-term variations of the global momentum flux distribution are discussed. GWs likely contribute significantly to the equatorward tilt of the polar night jet and to the poleward tilt of the summertime mesospheric jet. Our results suggest that GWs can undergo large latitudinal shifts while propagating upward. In particular, GWs generated by deep convection in the subtropical monsoon regions probably contribute significantly to the mesospheric summertime wind reversal at mid- and high latitudes. Variations in the GW longitudinal distribution caused by those convectively generated GWs are still observed in the mesosphere and could be important for the generation of the quasi two-day wave. Indications for quasi-biennial oscillation (QBO) induced variations of GW momentum flux are found in the subtropics. Also variations at time scales of about one 11-year solar cycle are observed and might indicate a negative correlation between solar flux and GW momentum flux.

Citation: Ern, M., P. Preusse, J. C. Gille, C. L. Hepplewhite, M. G. Mlynczak, J. M. Russell III, and M. Riese (2011), Implications for atmospheric dynamics derived from global observations of gravity wave momentum flux in stratosphere and mesosphere, *J. Geophys. Res.*, *116*, D19107, doi:10.1029/2011JD015821.

1. Introduction

[2] Gravity waves (GWs) are mesoscale waves with horizontal wavelengths of about a few tens up to several thousand km. They are excited by a number of different source processes. One source process is wave excitation by atmospheric flow over mountainous terrain. These orographically forced waves are also called mountain waves. The other source processes are called non-orographic and comprise, for example, GWs excited by wind jets (e.g., geostrophic adjustment) or GWs generated by deep convection, in particular in the tropics and subtropics.

[3] GWs are one of the most important coupling processes in atmospheric dynamics. They carry momentum from their source regions that are mostly located in the troposphere toward higher altitudes and accelerate or decelerate the atmospheric background flow when they dissipate. The key quantity relevant for this vertical coupling is the vertical flux of horizontal momentum:

$$\left(F_{px}, F_{py}\right) = \rho \left(\overline{u'w'}, \overline{v'w'}\right) \quad (1)$$

with F_{px} the vertical flux of zonal and F_{py} the vertical flux of meridional momentum. ρ is the atmospheric density, (u, v, w) the atmospheric background wind vector with u the zonal, v the meridional and w the vertical component, and (u', v', w') the vector of wind perturbations due to GWs. The overbar indicates spatial or temporal averaging over at least one wave

[1]Institut für Energie- und Klimaforschung – Stratosphäre, Forschungszentrum Jülich, Julich, Germany.
[2]Center for Limb Atmospheric Sounding, University of Colorado at Boulder, Boulder, Colorado, USA.
[3]National Center for Atmospheric Research, Boulder, Colorado, USA.
[4]Atmospheric, Oceanic, and Planetary Physics, Department of Physics, University of Oxford, Oxford, UK.
[5]NASA Langley Research Center, Hampton, Virginia, USA.
[6]Center for Atmospheric Sciences, Hampton University, Hampton, Virginia, USA.

0148-0227/11/2011JD015821

period. In the following, for convenience, the vector (F_{px}, F_{py}) is simply called momentum flux. The acceleration (X, Y) of the background flow is given by the vertical gradient of the momentum flux:

$$(X, Y) = -\frac{1}{\rho}\frac{\partial(F_{px}, F_{py})}{\partial z} \quad (2)$$

with X the zonal and Y the meridional acceleration. A more detailed discussion is given, for example, by *Fritts and Alexander* [2003].

[4] GWs are highly relevant for a number of processes in the stratosphere. For example, the quasi-biennial oscillation (QBO) of the zonal wind in the tropics is mainly driven by GWs. This is indicated by theoretical considerations and model studies [e.g., *Dunkerton*, 1997; *Kawatani et al.*, 2010a, 2010b], as well as by observations [e.g., *Ern and Preusse*, 2009a, 2009b; *Alexander and Ortland*, 2010]. The QBO has influence on the stratospheric polar winter jets [*Holton and Tan*, 1980] and by downward coupling also on the weather in the troposphere [e.g., *Baldwin and Dunkerton*, 1999, 2001; *Marshall and Scaife*, 2009]. GWs are also likely the main drivers of the westerly phase of the semi-annual oscillation (SAO) of the zonal wind in the tropics in the upper stratosphere [e.g., *Ray et al.*, 1998]. They are also important for the Brewer Dobson (BD) circulation [*Brewer*, 1949; *Dobson*, 1956] in the stratosphere, which is directed upward in the tropics, from the equator to the poles at midlatitudes, and downward over the poles. Recent simulations of a number of general circulation models (GCMs) predict an acceleration of the BD circulation in a warming climate [e.g., *Garcia and Randel*, 2008; *Li et al.*, 2008] and it is indicated that large part of this acceleration is due to changes in the propagation of mountain waves [*McLandress and Shepherd*, 2009].

[5] In the mesosphere GWs are even more important. They are the main drivers of the reversal of the mesospheric summer and winter jets [e.g., *Holton*, 1982, 1983] and they are responsible for the residual mesospheric circulation from pole to pole and the cold summer mesopause. There are also indications for interhemispheric coupling by GWs [*Becker and Fritts*, 2006] with possible effects for the occurrence of polar mesospheric clouds [*Karlsson et al.*, 2009].

[6] Because of their importance for atmospheric dynamics the effect of GWs has to be included in GCMs. Since the horizontal scales of GWs are too short to be fully resolved by GCMs, the effect of GWs on the atmospheric background flow has to be accounted for by gravity wave drag (GWD) parameterizations. Often in GCMs at least two different GW parameterizations are used: one for orographically generated GWs, and another parameterization for nonorographic GWs. The latter is intended to cover all other GW sources but is usually not directly linked to physical source processes. Also in weather prediction models GWD parameterizations are now being included to provide a more reliable upper atmosphere [e.g., *Orr et al.*, 2010]. Some standard nonorographic GWD parameterizations that are commonly used are, for example, the ones by *Lindzen* [1981], *Hines* [1997a, 1997b], *Alexander and Dunkerton* [1999], *Warner and McIntyre* [1996], or *Scinocca* [2003]. There are only very few examples of GCMs that resolve part of the GW spectrum and do not need a GWD parameterization [e.g., *Becker and Fritts*, 2006; *Watanabe et al.*, 2008]. However, those models are still computationally too expensive to be used for longer-term runs or even climate predictions. Therefore, GCMs will have to rely on GWD parameterizations in the near and mid-term future [e.g., *Kim et al.*, 2003].

[7] GWD parameterizations that are not linked to physical sources, in particular standard nonorographic GWD schemes, usually launch GW momentum flux vertically from a given source level. At this level source parameters have to be prescribed, for example, the source momentum flux, horizontal and/or vertical wavelengths, or the shape of the GW spectrum. However, there are only very few observations that provide useful constraints for GWD schemes. Therefore, the GW source parameters usually are guessed or tuned for the desired model response. Often no temporal (seasonal) variations of the sources are included. In addition, the physics of GW propagation is usually simplified. One of the main shortcomings in most GWD parameterizations is that only vertical propagation of GWs is considered.

[8] Therefore, there is an urgent need for global observations of, for example, GW amplitudes, horizontal and vertical wavelengths and, in particular, GW momentum flux that can directly be compared to the GWD parameterizations. Recently, to provide more reliable GW source distributions, some attempts have been made to couple the GW source spectrum of GWD parameterizations in GCMs to physical processes [e.g., *Charron and Manzini*, 2002; *Song and Chun*, 2008; *Richter et al.*, 2010]. Also those approaches are in need of validation by global observations.

[9] An overview of global observation techniques for GWs and in particular GW momentum flux is, for example, given by *Preusse et al.* [2008] or, including also in situ techniques, by *Alexander et al.* [2010]. Global observations can only be provided by satellite measurements. First observations of GWs from satellite were made by *Fetzer and Gille* [1994] using Limb Infrared Monitor of the Stratosphere (LIMS) observations. On the basis of Cryogenic Infrared Spectrometers and Telescopes for the Atmosphere (CRISTA) temperature measurements global distributions of GW momentum fluxes from satellite data were derived for the first time by [*Ern et al.*, 2004] and some constraints for GWD parameterizations were deduced [*Ern et al.*, 2005, 2006]. Following the demand for further observations, global distributions of GW momentum flux were also derived from temperatures of Global Positioning System Radio Occultations (GPS-RO) [*Fröhlich et al.*, 2007] adopting the CRISTA GW horizontal wavelength distribution. Most recently, global distributions of GW momentum flux were estimated from temperatures measured by the High Resolution Dynamics Limb Sounder (HIRDLS) instrument [*Alexander et al.*, 2008; *Wright et al.*, 2010]. All these studies provide only absolute values of GW momentum flux, i.e., no direction. First attempts have been made to derive even the direction of GW momentum flux from GPS-RO temperatures [*Wang and Alexander*, 2010]. However, the horizontal sampling of the existing satellite instruments is still too sparse to provide reliable results.

[10] In our study we combine the approach by *Ern et al.* [2004] with an improved removal of the global-scale atmospheric background to obtain the smaller-scale temperature fluctuations of GWs. This approach is based on a

two-dimensional Fourier decomposition in longitude and time and covers also shorter-period planetary-scale waves with periods as short as 1–2 days, resulting in improved stratospheric GW momentum flux distributions and, even more important, in an extension of the altitude range into the mesosphere.

[11] We derive absolute values of GW momentum fluxes for the high-resolution data set of HIRDLS temperatures that cover the upper troposphere and the full stratosphere. In addition, we derive for the first time global distributions of GW momentum fluxes in the mesosphere for the almost 9-year-long data set of Sounding of the Atmosphere using Broadband Emission Radiometry (SABER) temperature observations that cover both stratosphere and mesosphere. By combining these two data sets we investigate seasonal and longer-term variations of GW momentum flux in stratosphere and mesosphere.

[12] A short description of the CRISTA, HIRDLS and SABER instruments is given in section 2. In section 3 the methods for the removal of the global-scale atmospheric background and the estimation of GW momentum flux absolute values from HIRDLS and SABER observations are introduced. In section 4 these momentum flux results are compared to the CRISTA momentum flux observations by *Ern et al.* [2004] as a reference. Seasonal variations in stratosphere and mesosphere and implications for the dynamics of the mesosphere are discussed in section 5. Longer-term variations are discussed in section 6. Consequences for the dynamics of the mesosphere caused by the non-uniform longitudinal distribution of GW momentum flux are discussed in section 7. A summary of our results is given in section 8.

2. The Instruments CRISTA, HIRDLS, and SABER

[13] Our study is mainly based on temperature data of the three infrared limb sounding satellite instruments CRISTA, HIRDLS and SABER, which will be briefly introduced in the following. The fact that all three instruments are limb sounders is a prerequisite for all our analyses because only this viewing geometry provides the high vertical resolution needed to cover atmospheric waves over a range of vertical wavelengths as large as possible. In our analyses we focus on the temperature measurements of these instruments only. It should however be noted that all instruments also provide measurements of a number of trace species.

[14] The observational filter for limb sounding of optically thin emissions from satellite has been discussed in detail by *Preusse et al.* [2002, 2009a]. Only GWs with horizontal wavelengths longer than about 100–200 km are visible for infrared limb sounders (also depending on vertical wavelength). The shortest vertical wavelengths visible are largely determined by the instantaneous vertical field of view of the satellite instrument. For example, with an about 1 km vertical field of view HIRDLS can see GWs with vertical wavelengths longer than about 2 km. SABER and CRISTA have a wider vertical field of view and the detection threshold is shifted to somewhat longer vertical wavelengths: SABER can detect GWs with vertical wavelengths >4 km and CRISTA vertical wavelengths longer than about 5 km.

2.1. CRISTA

[15] The CRISTA instrument was part of two Space Shuttle missions in November 1994 (CRISTA-1) and August 1997 (CRISTA-2). Measurements are available for the periods 4–12 November 1994 for CRISTA-1 and 8–15 August 1997 for CRISTA-2. An overview over these two missions is given in *Offermann et al.* [1999] and *Grossmann et al.* [2002]. Atmospheric temperatures were derived from CO_2 infrared limb emissions at 12.6 μm [*Riese et al.*, 1997, 1999]. During these two one-week measurement periods the CRISTA instrument provided high resolution atmospheric measurements in all three spatial directions. Especially the horizontal measurement grid was largely improved by using three viewing directions simultaneously. In addition, very short distances between subsequent altitude profiles along the satellite measurement tracks were achieved by helium cooling of the instrument. During CRISTA-1 along-track distances were especially short (about 200 km) from 5–8 November 1994 and on 11 November 1994. During CRISTA-2 measurements with short along-track distances (about 240 km) were taken from 9–13 August 1997 and partly on 8, 14 and 15 August 1997. From these periods global snapshots of GW momentum flux absolute values were derived [*Ern et al.*, 2004, 2006]. The latitudinal coverage is about 57°S to 66°N for CRISTA-1 and about 72°S to 72°N for CRISTA-2.

2.2. HIRDLS

[16] The HIRDLS instrument is one of the core instruments onboard the Aura spacecraft of the Earth Observing System (EOS) program. The EOS-Aura spacecraft was launched on 15 July 2004. During launch large part of the HIRDLS optical aperture became obscured by a piece of plastic film and it was not possible to make use of the horizontal scanning capabilities as planned. Instead, the instrument was operated with the viewing direction fixed to an azimuth of −47° with respect to the orbit plane, i.e., in a northward looking viewing geometry, resulting in a latitudinal coverage of about 63°S to 80°N.

[17] Atmospheric temperatures are derived from 15 μm CO_2 infrared emissions using several narrow spectral channels. Perturbations of the measured atmospheric limb radiances that occurred because of the partial obscuration of the HIRDLS field of view have been effectively removed [*Gille et al.*, 2008]. Along-track distances between subsequent altitude profiles are extremely short (about 100 km) owing to the fact that HIRDLS was operated with the viewing direction fixed to a single azimuth. Especially for the analysis of GWs this extremely fine along-track sampling is an invaluable benefit (see also section 3).

[18] In our study we use HIRDLS version V005 data, which are available for the period January 2005 until December 2007. More detailed information about the HIRDLS instrument is given, for example, by *Gille et al.* [2003, 2008].

2.3. SABER

[19] The SABER instrument was launched onboard the Thermosphere Ionosphere Mesosphere Energetics and Dynamics (TIMED) satellite in December 2001. Designed especially for measurements at higher altitudes the SABER

instrument measures temperatures in an altitude range from the tropopause to well above 100 km. Like for HIRDLS the SABER temperatures are derived from 15 μm CO_2 infrared emissions. Details of the temperature retrieval are given, for example, by *Remsberg et al.* [2004, 2008].

[20] Due to solar angle restrictions the TIMED satellite performs yaw maneuvers every about 60 days. Consequently, the SABER viewing geometry shifts between a northward viewing geometry, covering latitudes between about 50°S and 82°N, and a southward viewing geometry, covering the latitude range between about 82°S and 50°N. The viewing direction is always perpendicular to the orbital plane.

[21] In our study we use version 1.07 SABER data. Data are available starting from January 2002 and measurements are still ongoing. This means that the SABER data are a real long-term data set that meanwhile covers almost a full 11-year solar cycle with an excellent instrument stability. Further information about the SABER instrument is given, for example, by *Mlynczak* [1997] or *Russell et al.* [1999].

3. Estimation of Gravity Wave Momentum Flux Absolute Values

[22] The method to derive GW momentum fluxes is a two-step procedure that has first been described by *Ern et al.* [2004]. In the first step the atmospheric background state consisting of the zonal mean temperature profile as well as global-scale waves has to be removed from the measured temperature altitude profiles. The result are profiles of residual temperatures that can be attributed to short horizontal scale atmospheric fluctuations, mostly GWs. In the second step a vertical wave analysis is performed for these altitude profiles of residual temperatures and absolute values of GW momentum fluxes can be estimated for pairs of altitude profiles.

3.1. Removal of the Atmospheric Background

3.1.1. Previous Methods

[23] Several techniques have been employed to separate the short horizontal scale GWs from the global-scale atmospheric background state. Some of them are briefly summarized here.

[24] One method is vertical high-pass filtering of temperature altitude profiles. Global-scale waves often have longer vertical wavelengths than GWs so that short vertical wavelength GWs can be separated from global-scale waves by high-pass filtering [e.g., *de la Torre et al.*, 2006]. This method is however limited to GWs with vertical wavelengths shorter than about 10 km. In addition, global-scale waves can also have short vertical wavelengths (e.g., Kelvin waves in the tropics) so that GWs cannot always be cleanly separated.

[25] Therefore, several other methods determine the global-scale atmospheric background state by means of a global horizontal wave analysis. For example, global-scale waves with zonal wavenumbers 0–6 have been estimated using a Kalman filter method [e.g., *Fetzer and Gille*, 1994; *Ern et al.*, 2004]. In another approach global-scale waves with zonal wavenumbers 1–3 were estimated using an S-transform [e.g., *Alexander et al.*, 2008; *Wright et al.*, 2010].

[26] These different approaches have been proven to work well in many cases in the stratosphere. However, in our study we also want to estimate GW momentum fluxes in the mesosphere where frequently global-scale waves with very short periods of only a few days are observed, for example quasi two-day waves or fast Kelvin waves [e.g., *Garcia et al.*, 2005; *Ern et al.*, 2009a].

[27] Therefore, a new method to remove the atmospheric background has been developed that covers also those short-period global-scale waves in the mesosphere and, because of a better exploitation of the satellite viewing geometry, provides improved results also in the stratosphere, especially in the tropics and the wintertime polar vortices. This new method is based on a two-dimensional Fourier decomposition of the satellite data in longitude and time and will be described in the following.

3.1.2. Longitude-Time 2d-Fourier Decomposition

[28] The global sampling patterns of satellite instruments in low Earth orbit are largely governed by orbital mechanics. With a single fixed viewing direction it is possible to resolve global-scale waves with zonal wave numbers as high as 6–7 and wave frequencies of up to about 1 cycle/day within the Nyquist limits, if measurements from both ascending and descending orbit branches (i.e., measurements from overpasses with increasing and decreasing geographical latitude) are combined [e.g., *Salby*, 1982a, 1982b]. This characteristic sampling geometry is called twice-daily asynoptic sampling [*Salby*, 1982a, 1982b]. The resulting measurement grid on a fixed latitude circle is not regular and equispaced in longitude and time. Nevertheless, it is possible to perform two-dimensional Fourier analyses in longitude and time for a given latitude and altitude. Different types of global-scale waves often have characteristic spectral peaks in longitude-time spectra and can therefore easily be identified and separated by band-pass filtering. Therefore, 2d-Fourier analysis has been successfully applied for investigation of global-scale waves [e.g., *Lait and Stanford*, 1988a, 1988b; *Wu et al.*, 1996; *Garcia et al.*, 2005; *Ern et al.*, 2008, 2009a, 2009b; *Ern and Preusse*, 2009a, 2009b].

[29] Different from this, GWs have too short horizontal scales and are too intermittent in nature to be resolved by the twice-daily asynoptic sampling pattern. Therefore, the spectral contribution of GWs appears as a uniform white-noise background-level in longitude-time spectra [e.g., *Ern et al.*, 2008]. This completely different spectral behavior can be utilized for a new method to separate planetary-scale waves from GWs.

[30] Like in our previous studies this new method is based on longitude-time Fourier spectra that are calculated for a set of time windows, each 31 days long, on a set of fixed latitudes and altitudes after removal of the zonal mean temperature and a linear temperature trend [e.g., *Ern et al.*, 2008]. The choice of 31-day time windows is a good compromise. On one hand, the window length of 31 days is sufficient to resolve seasonal variations of the zonal mean atmospheric state. On the other hand, this length of the time windows offers a good spectral resolution and the spectral contributions of global-scale wave modes can be isolated.

[31] We use overlapping 31-day time windows with time steps of about 15 days. This has the advantage that for most altitude profiles we can calculate two estimates for the global-scale atmospheric background temperature. By

combining these estimates boundary effects at the edges of the time windows are minimized. The procedure how the atmospheric background is estimated is described in detail below. Only for SABER time windows are chosen non-overlapping when SABER changes from northward to southward viewing geometry or vice versa (i.e., every about 60 days).

[32] For our analysis, the data of the HIRDLS and SABER instruments are linearly interpolated to a fixed set of latitudes and altitudes. For HIRDLS spectral analyses are carried out for latitudes from 63°S to 80°N in 1-degree steps and for altitudes from 5 km to 80 km in 0.5 km steps. Also for the SABER instrument a latitudinal step of 1° is chosen. The time windows are defined in a way not to mix the northward and the southward viewing geometries of SABER. The latitudinal coverage is therefore either 50°S to 82°N or 82°S to 50°N. The set of fixed altitudes used for SABER is 14 to 125 km in 1 km steps.

[33] Similarly to *Ern et al.* [2008], we estimated the uniform white-noise spectral background-level due to GWs in the squared spectral amplitudes. Spectral amplitudes are assumed to be due to global-scale waves if the squared spectral amplitude exceeds the white-noise level by a factor of at least 5. These spectral amplitudes are then corrected for the offset caused by the white-noise.

[34] The choice of the threshold value of a factor of 5 is somewhat arbitrary. Spectral components of global-scale waves that are below this threshold cannot be distinguished from the white-noise spectral contributions and are therefore neglected. However, because of the small temperature variance contained in those components, this has only little effect on the estimation of the global-scale background temperatures and the derived residual temperatures that can mainly be attributed to GWs.

[35] For our atmospheric background estimation we utilize the following spectral range: zonal wavenumbers 0–6 and wave frequencies up to 0.7 cycles/day. This spectral range covers the largest part of the spectral domain that can be resolved by the twice daily asynoptic satellite sampling (a tilted rectangle in the zonal wavenumber/frequency domain [see also *Salby*, 1982a, 1982b]). In addition, the two strongest tidal components present in the stratosphere and mesosphere [e.g., *Forbes et al.*, 2006; *Mukhtarov et al.*, 2009; *Pancheva et al.*, 2010] are accounted for: the diurnal westward tide with zonal wavenumber one (shortly called DW1 tide), as well as the diurnal eastward tide with zonal wavenumber 3 (shortly called DE3 tide).

[36] The removal of tides poses a general problem: Due to the Nyquist limitations of our space-time spectra not all eastward and westward propagating diurnal tidal modes can be resolved unambiguously, and there will be spectral aliasing between eastward and westward propagating diurnal tides. Therefore we chose to only remove the DW1 and the DE3 diurnal tides, i.e. the dominant tidal spectral components in the mesosphere, which are only little affected by spectral aliasing.

[37] This approach may be sufficient below about 90 km altitude, where the DW1 and the DE3 tides are the dominant tidal modes. However, at altitudes above 90 km also other tidal modes can attain large amplitudes [e.g., *Forbes et al.*, 2006; *Pancheva et al.*, 2010]. These tides are not resolved by our space-time spectra and have to be neglected. Consequently, our GW analysis will be less reliable and subject to larger errors above about 90 km altitude.

3.1.3. Determination of Residual Temperatures Due to Gravity Waves

[38] Residual temperatures are calculated separately for each altitude profile and each altitude of this altitude profile. The procedure is as follows: First, the closest latitudes and altitudes for which space-time spectral analyses were calculated are identified and the spectra are interpolated in a linear way to obtain an optimum spectrum for the desired location. Then for the longitude and time of the measurement an estimate for the superposition of the global-scale waves is calculated based on the spectral amplitudes and phases of only the spectral components that exceed the threshold value mentioned above. This procedure is similar to the evaluation of a Hovmöller diagram (i.e., a longitude-time cross section) like the ones shown by *Ern et al.* [2008] for a given longitude and time. The local background temperature is then obtained by adding the mean background temperature (31-day average plus linear trend) and the superposition of global-scale waves.

[39] For most altitude profiles two local background temperature estimates are available because of the overlapping time windows. We calculate a weighted average of these background estimates with the relative weight of a single estimate linearly decreasing with the time difference between the center time of the spectral analysis window and the time of observation of the altitude profile considered. The weight is zero if the time difference exceeds 15.5 days, i.e., half the width of an analysis window. Finally, by subtracting these average local background temperatures from the measurements we obtain altitude profiles of residual temperatures that are dominated by GWs.

[40] Two additional corrections are applied to these residual temperatures. In a few cases data gaps in the satellite sampling pattern lead to some aliasing and leakage in the calculated space-time spectra, causing sometimes inaccuracies in the estimation of the global-scale atmospheric background state. Especially in some cases for SABER at high latitudes during wintertime there are still some temperature residuals due to quasi-stationary planetary waves remaining after removal of the 2d-Fourier global-scale atmospheric background state. Therefore, for a further cleanup, in each altitude profile the dominant vertical oscillation with vertical wavelength $\geq$40 km is removed, which effectively reduces the remaining residuals due to quasi-stationary planetary waves. In other cases this correction has only little effect on the residual temperatures. The second correction is only applied to SABER data: Above 60 km SABER altitude profiles are low-pass filtered with a vertical cutoff wavelength of 5 km to remove very short-scale vertical oscillations around the mesopause that are likely a retrieval artifact. Also this correction has little effect on the residual temperatures due to GWs because at higher altitudes the dominant GWs usually have longer vertical wavelengths.

3.2. Vertical Analysis and Calculation of Momentum Fluxes

[41] The method to determine GW momentum fluxes that is employed in our study has been described before in detail by *Ern et al.* [2004] and is only shortly summarized here.

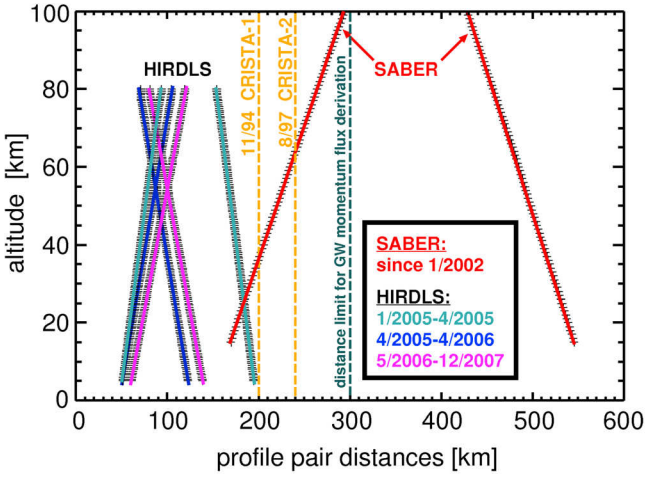

Figure 1. Distances between subsequent altitude profiles along the measurement track for the instruments CRISTA, HIRDLS and SABER as function of measurement altitude. While CRISTA measures almost vertical altitude profiles, resulting in equispaced along-track distances, HIRDLS and SABER use a triangular vertical scan pattern, resulting in alternating shorter-distance and longer-distance pairs of altitude profiles along the measurement track. For details see text.

[42] For each measured altitude profile of residual temperatures a vertical analysis is carried out. A set of dominant vertical wavelengths is determined for each altitude profile by Maximum Entropy Method (MEM). The spectral analysis is carried out by MEM, because the MEM offers a better spectral resolution than, for example, a fast Fourier transform (FFT). For each altitude the amplitude, vertical wavelength, as well as the phase of the dominant wave are then determined by sine-fitting in a vertical window centered at the altitude level considered. In our study a 10 km vertical window is used. The result are altitude profiles of wave amplitudes, vertical wavelengths and phases. This procedure has been called MEM-HA method and is described in detail by *Preusse et al.* [2002].

[43] If the horizontal distances along the measurement track between subsequent altitude profiles are sufficiently short, it can be assumed that in both altitude profiles of a profile-pair the same GW has been measured. In this case also the horizontal wavelength of the GW can be calculated from the vertical phase shift of the wave structures seen in both profiles. Since both profiles are measured quasi-instantaneously (within 35 seconds or less) observed phase shifts are fully attributed to the horizontal structure of an observed GW. For a given distance dl between the profiles and an observed phase shift $d\Phi$ of the vertical structures, the horizontal wavelength λ_h along the measurement track is:

$$\lambda_h = 2\pi/k_h = 2\pi\, dl/d\Phi \tag{3}$$

Usually the satellite measurement track and the wave vector of the observed GW are not aligned. Therefore, the values of λ_h will usually overestimate the true wavelength of the GW. In particular, from only pairs of altitude profiles it is not possible to determine the propagation direction of the waves. Only the projection k_h of the horizontal wave vector on the measurement track can be determined, not the wave vector itself. This is illustrated in more detail in *Preusse et al.* [2009a]. Therefore, following *Ern et al.* [2004], only absolute values of GW momentum flux (no direction) can be calculated via the following equation:

$$F_{ph} = \frac{1}{2}\,\rho\,\frac{k_h}{m}\left(\frac{g}{N}\right)^2\left(\frac{\hat{T}}{T}\right)^2 \tag{4}$$

In this equation ρ is the density of the background atmosphere, g the gravity acceleration, N the buoyancy frequency, k_h the horizontal and m the vertical wavenumber of the GW, $\hat{T}$ the temperature amplitude of the wave, and T the background temperature.

[44] Because of the observational filter that applies for optically thin emissions in limb viewing geometry, only GWs with horizontal wavelengths longer than about 100–200 km can be observed [e.g., *Preusse et al.*, 2002, 2009a]. Therefore, the Nyquist theorem implies that the sampling should be denser than 50–100 km for resolving all waves observed. Previous detailed investigations [*Ern et al.*, 2004] have shown, however, that in a statistical sense the horizontal wavelength distribution can be reasonably well captured up to a profile distance of about 300 km. We therefore tentatively apply this limit and the results discussed below confirm this approach.

[45] For the CRISTA, HIRDLS and SABER instruments the along-track distances between subsequent altitude profiles are given as function of measurement altitude in Figure 1. CRISTA measured almost vertical altitude profiles by viewing backward with respect to the flight direction and scanning always from high to low tangent altitudes [e.g., *Riese et al.*, 1999], resulting in altitude-independent along-track distances of about 200 km during CRISTA-1 and about 240 km during CRISTA-2. HIRDLS and SABER have a triangular vertical scan pattern, resulting in pairs of altitude profiles with alternating shorter and longer distances along the measurement track. From Figure 1 it can be seen that along-track distances for CRISTA and all HIRDLS scanning modes are well below the 300 km threshold required for determination of GW momentum fluxes. However, due to altitude restrictions of the vertical scanning modes or data quality, for these instruments GW momentum fluxes can only be derived in the stratosphere. For SABER the 300 km criterion is fulfilled only for the short-distance pairs of altitude profiles. But for these short-distance pairs it is possible to derive momentum fluxes up to altitudes of about 100 km, covering the whole mesosphere.

[46] Momentum fluxes derived for only short and only long HIRDLS altitude profile pair distances separately give some information about uncertainties that arise from horizontal undersampling of GWs. Especially during the first months of HIRDLS observations, i.e., when differences between short and long distances are especially large (see Figure 1; about a factor of 3 at 20 km altitude), these momentum fluxes can differ by as much as about a factor of two, which is about what is expected from considerations by *Ern et al.* [2004]. The magnitude of this difference is qualitatively in agreement with the correction for horizontal undersampling of waves applied to the CRISTA momentum fluxes from *Ern et al.* [2004] and could be

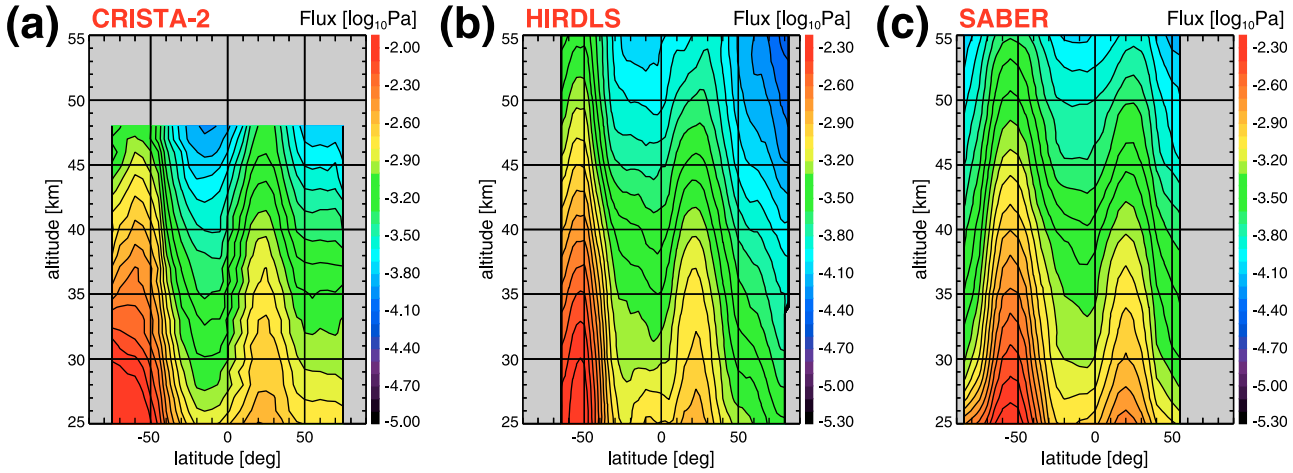

Figure 2. Zonal cross sections of gravity wave momentum flux absolute values for (a) CRISTA-2 in August 1997, as well as for (b) HIRDLS and (c) SABER in August 2006. Values are given in $\log_{10}$ (Pa). Please note the different latitudinal coverage of the three instruments. For details see text.

understood as some kind of confirmation for this highly uncertain correction.

4. Comparison to CRISTA Momentum Fluxes

[47] Before we start with the discussion of spatial and temporal variations of HIRDLS and SABER data in the next sections, as a first cross-check, we compare GW momentum fluxes derived from HIRDLS and SABER to the earlier CRISTA values. CRISTA GW momentum fluxes have been validated with results obtained by superpressure balloons, an independent in situ measurement technique. This comparison shows very good agreement between CRISTA and in situ GW momentum fluxes [*Hertzog et al.*, 2008]. Therefore, CRISTA momentum fluxes can be used as a reference for HIRDLS and SABER.

[48] The calculation of GW momentum fluxes for HIRDLS and SABER in our study is very similar to the study by *Ern et al.* [2004] using CRISTA data. The main difference is the determination of the global-scale atmospheric background, which was carried out by a Kalman filter in *Ern et al.* [2004], and which is now performed by 2d-Fourier method. In addition, we now use a vertical wavelength range of 2–25 km, which is somewhat larger than the 5–25 km used for CRISTA-1 and the 6–30 km used for CRISTA-2. This larger range is possible because the retrieved HIRDLS and SABER temperatures contain also somewhat shorter vertical wavelengths than the CRISTA temperatures.

[49] Especially suited for a comparison to HIRDLS and SABER momentum fluxes are the data from the CRISTA-2 mission in August 1997. This is the case because in August 2006, a month covered by both HIRDLS and SABER, the global meteorological conditions are very similar. In particular, in August 2006 the QBO phase is the same as in August 1997 (QBO eastward phase at 30 hPa). In addition, the global distribution of GW momentum flux in August usually has very characteristic features: enhanced momentum fluxes in the well developed southern polar vortex and over the monsoon regions in the northern hemisphere.

[50] For a meaningful comparison only vertical wavelengths longer than 6 km are considered to approximately match the vertical wavelength range of CRISTA-2. In addition, for HIRDLS and SABER also the same vertical wavelength matching criterion as for CRISTA is applied to make sure that in both altitude profiles of a considered profile-pair the same GW is observed. For CRISTA the vertical wavelengths in the two profiles of a considered pair were allowed to differ by as much as 6 km. Please note, that in the following sections this criterion is not longer used and replaced by a criterion based on relative deviations. This makes more sense for HIRDLS and SABER because also shorter vertical wavelengths are covered (see below).

[51] Figure 2 shows zonal mean cross sections of GW momentum flux absolute values for CRISTA-2 (Figure 2a), as well as for HIRDLS (Figure 2b) and SABER (Figure 2c). Figure 2a represents one week in August 1997, while Figures 2b and 2c are monthly averages over the whole month of August 2006.

[52] All three zonal cross sections show very similar relative structures. There is a maximum at high latitudes in the southern hemisphere, corresponding to high GW momentum fluxes in the southern winter polar vortex. Another maximum can be found in the northern subtropics, corresponding to enhanced GW momentum flux over the monsoon regions on the summer hemisphere. The color scales for HIRDLS and SABER (Figures 2b and 2c) are exactly the same and values agree within about one color level (i.e., about 30%). Only in the southern polar vortex HIRDLS momentum fluxes are somewhat higher than SABER values. The reason could be the different latitudinal coverage of HIRDLS and SABER, or the shorter along-track sampling distance of HIRDLS allows to resolve shorter horizontal wavelength GWs, resulting in higher (more accurate) GW momentum flux values where short horizontal wavelength GWs are dominant.

[53] The color scale for CRISTA (Figure 2a) is shifted toward higher values by a factor of two. This means that CRISTA momentum fluxes show the same relative structures, but are up to a factor of two higher than the HIRDLS and SABER values. This offset is as expected because for calculating CRISTA GW momentum fluxes two additional corrections were applied [*Ern et al.*, 2004]. First, the

damping of wave amplitudes due to radiative transfer and retrieval algorithm was corrected. This correction has been derived from detailed retrieval studies by *Preusse et al.* [2002] and has been validated in a case study by comparison to low miss-distance radiosonde observations so that CRISTA and the radiosondes observed the same GWs during the satellite overpasses [*Preusse et al.*, 2003]. The second correction was applied to correct for the undersampling of GWs by the CRISTA measurement grid.

[54] Both corrections are not applied to the HIRDLS and SABER data because the retrieval sensitivity of the HIRDLS and SABER retrievals to observed GWs has not been studied so far. In addition, the undersampling of waves should be less severe than for the CRISTA-2 data because of the shorter profile pair distances of HIRDLS and SABER, at least in the stratosphere.

[55] A detailed error discussion of GW momentum flux absolute values is given by *Ern et al.* [2004]. Errors are at least about a factor of two, even if corrections for retrieval sensitivity and horizontal undersampling of waves are applied, like for CRISTA. Very conservative error estimates result in even larger error ranges.

5. Seasonal Variations of Gravity Wave Parameters in Stratosphere and Mesosphere

[56] In this section we will investigate seasonal variations of HIRDLS and SABER GW parameters, in particular GW momentum fluxes. We focus on the year 2006 because previous studies by *Alexander et al.* [2008] and *Yan et al.* [2010] based on HIRDLS data also focus on this year and results can be compared.

[57] In the following we utilize the full range of vertical wavelengths of 2–25 km covered by our method. To make sure that in both altitude profiles of a profile-pair the same GW is observed we use a vertical wavelength matching criterion different from the one used in section 4: Simulating the whole process chain of temperature retrieval followed by a MEM-HA vertical wavelength analysis *Preusse et al.* [2002] showed that the vertical wavelength of a GW present in an altitude profile can be reproduced with an accuracy of about ±20%. Given this accuracy, we now assume that in both altitude profiles of a profile-pair the same GW is observed if the vertical wavelengths of the dominant waves in the two profiles differ by no more than 40%. If not, then the profile pair is disregarded.

[58] Due to increased measurement noise above about 60 km the HIRDLS altitude range of GW momentum fluxes is from the tropopause to about 55–60 km. This means that the full stratosphere is covered by the high resolution HIRDLS data and seasonal variations of the horizontal distribution of GW momentum flux can be studied in great detail in the whole stratosphere for the three years (2005–2007) of HIRDLS data available.

[59] The SABER instrument has a longer horizontal sampling distance along the measurement track and GW momentum fluxes can only be derived from the shorter-distance pairs of altitude profiles. Therefore, the number of altitude profiles per day available for the calculation of momentum fluxes is about a factor of 8–10 lower than for HIRDLS. This means that SABER momentum flux distributions do not achieve the extremely high horizontal resolution of the HIRDLS data. On the other hand, given the low instrument noise of SABER at high altitudes, it is possible to derive GW momentum fluxes also in the whole mesosphere, up to altitudes of about 100 km. In addition, the SABER data set is now almost nine years long, allowing also longer-term variations of the global GW momentum flux distribution to be studied.

[60] Consequently, the data sets of both instruments combined provide an excellent opportunity to study both seasonal variations of GW momentum flux in detail, as well as longer-term variations in the stratosphere and, for the first time, also in the mesosphere.

5.1. Seasonal Variations of the Horizontal Distribution of Gravity Wave Momentum Flux in the Stratosphere

[61] Seasonal variations of the global horizontal distribution of GW activity have been studied before, for example, by *Jiang et al.* [2004a, 2004b] or *Preusse et al.* [2009b]. The high resolution HIRDLS data now offer a much better horizontal resolution and also seasonal variations of GW momentum fluxes can be investigated. Figure 3 shows horizontal maps of GW momentum flux for the HIRDLS instrument at 30 km altitude. The high resolution (10° longitude times 5° latitude) maps are monthly averages for January (Figure 3a), April (Figure 3b), July (Figure 3c), and November 2006 (Figure 3d).

[62] In January and July 2006 (Figures 3a and 3c), there are enhanced values of GW momentum flux especially at high latitudes of the respective winter hemisphere. Those GWs that are related to the polar night wind jets are likely a mixture of waves generated by a number of different source processes, for example, geostrophic adjustment or jet instabilities. In addition, also GWs generated by fronts or orography will play an important role.

[63] In the summer hemisphere there are several well localized maxima of GW momentum flux. These maxima are caused by GWs that are generated by deep convection in the monsoon regions. In addition, the specific circulation in the upper troposphere allows for better vertical propagation of GWs in these regions. In the southern hemisphere during January (Figure 3a) there are three strong momentum sources at about 20°S over South America, South Africa, and North Australia. In addition, there is also a weaker source region over the Pacific Ocean. In the northern hemisphere during July (Figure 3c) there are two strong momentum sources at about 25°N over the Gulf of Mexico and over Southeast Asia, and a third weaker one over North Africa. These characteristic maxima of GW activity have been observed before, for example, by *Jiang et al.* [2004b], *Ern et al.* [2004], or *Preusse et al.* [2009b].

[64] In the intermediate seasons (spring and autumn, Figures 3b and 3d) GW momentum flux is strongly reduced in the polar regions and there is only little indication for convectively generated GWs in the subtropics. One of the main momentum sources in these two seasons are mountain waves (i.e., GWs generated by large scale flow over mountainous terrain). By checking the dispersion relation for GWs, mountain waves have been identified in satellite observations for the first time by *Eckermann and Preusse* [1999] based on CRISTA temperature data. Another study was carried out later by *Jiang et al.* [2004a] using Upper

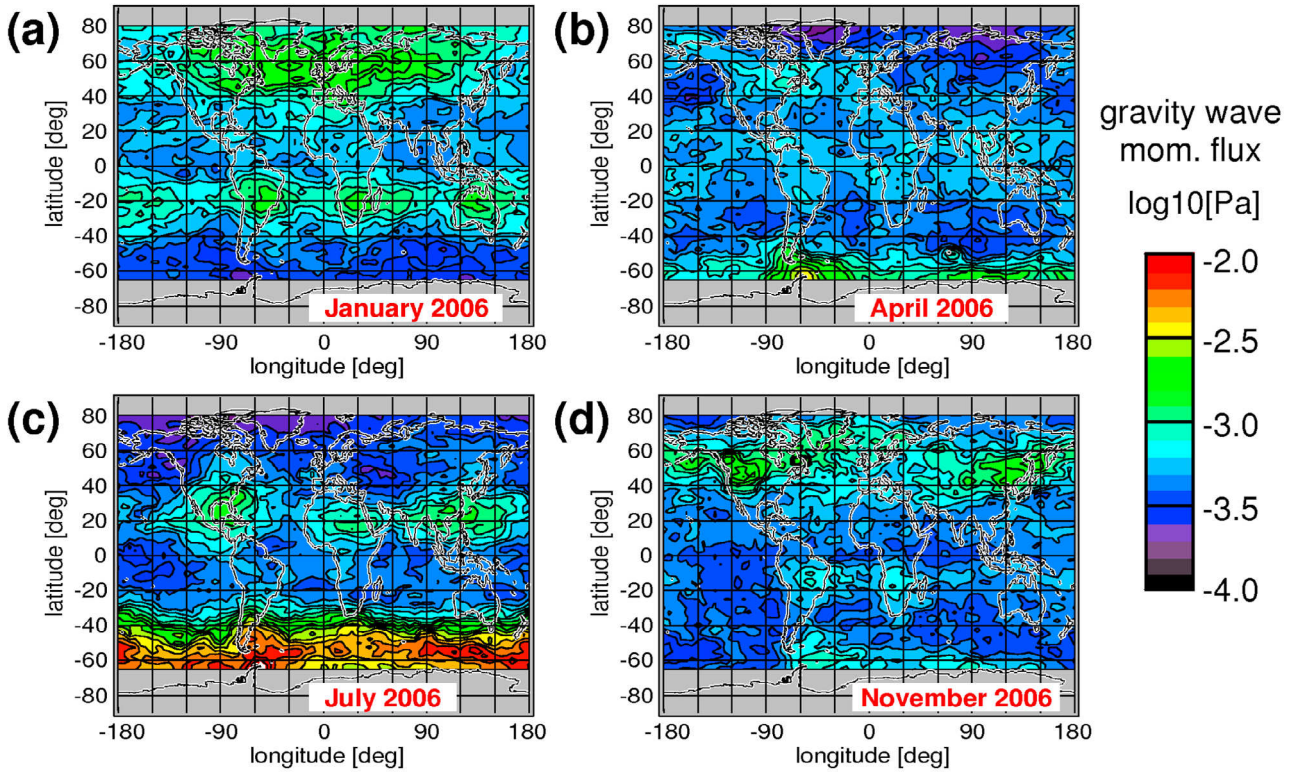

Figure 3. Average horizontal distribution of HIRDLS gravity wave momentum flux absolute values at 30 km altitude for (a) January, (b) April, (c) July, and (d) November 2006. Values are given in $\log_{10}$ (Pa). For details see text.

Atmosphere Research Satellite (UARS) Microwave Limb Sounder (MLS) data.

[65] In April (Figure 3b) high values of GW momentum flux are particularly found over the Southern Andes and Tierra del Fuego, as well as along the coast of Antarctica and sometimes over islands in the Southern Ocean, for example, in April 2006 over the Kerguelen Islands at about 50°S and 70°W. Only little mountain wave activity is found in the northern hemisphere.

[66] In November (Figure 3d) hot spots of mountain wave activity can be found in the whole northern midlatitudes, for example, over the Rocky Mountains, the northern Appalachian Mountains, Greenland, Scandinavia, the Urals, as well as the mountain ridges in Eastern Asia. This distribution of mountain waves in the northern hemisphere is qualitatively similar to the findings of *Jiang et al.* [2004a]. In the southern hemisphere there is still some mountain wave activity over the Southern Andes, Tierra del Fuego and the Antarctic coast, but less pronounced than in the study by *Eckermann and Preusse* [1999].

[67] The occurrence of these hot spots of GW momentum flux over mountain ridges indicates that, at least during part of the spring and autumn seasons, mountain waves can be the dominant source of GW momentum flux.

5.2. Seasonal Variations of the Vertical Distribution of Gravity Wave Parameters in Stratosphere and Mesosphere

[68] Figure 4 shows zonal mean GW squared amplitudes, vertical wavelengths, the reciprocal of the horizontal wavelength, as well as GW momentum fluxes for HIRDLS in January, April, July, and October 2006.

[69] Figure 5 shows the same for SABER, but for a larger altitude range. To allow a better comparison between the observations of both instruments we use the same vertical range of 25–100 km in both figures although HIRDLS covers only altitudes up to about 60 km. Areas not covered with data and values below the lowest value of the color scale are set to grey color in all panels of Figures 4 and 5.

[70] Because of the satellite yaw maneuvers latitudes poleward of 50° are covered only during part of the month by SABER measurements in January and July. SABER zonal averages are therefore less reliable at high latitudes in these months.

[71] For comparison contour lines of the Stratospheric Processes And their Role in Climate (SPARC) zonal wind climatology [*Randel et al.*, 2002; *Swinbank and Ortland*, 2003; *Randel et al.*, 2004] are overplotted in all panels of Figures 4 and 5. Dashed lines indicate westward and solid lines eastward wind. The contour increment is 10 m/s.

[72] Seasonal variations of the vertical distribution of GW parameters have also been discussed before in several studies. For example, seasonal variations of GW amplitudes and vertical wavelengths have been investigated in detail by *Yan et al.* [2010] for the year 2006 using HIRDLS data. In addition, HIRDLS GW amplitudes, vertical wavelengths, reciprocal horizontal wavelengths, and GW momentum fluxes for May 2006 are presented by *Alexander et al.* [2008]. In the following we will therefore focus on comparisons with those studies based on HIRDLS observations.

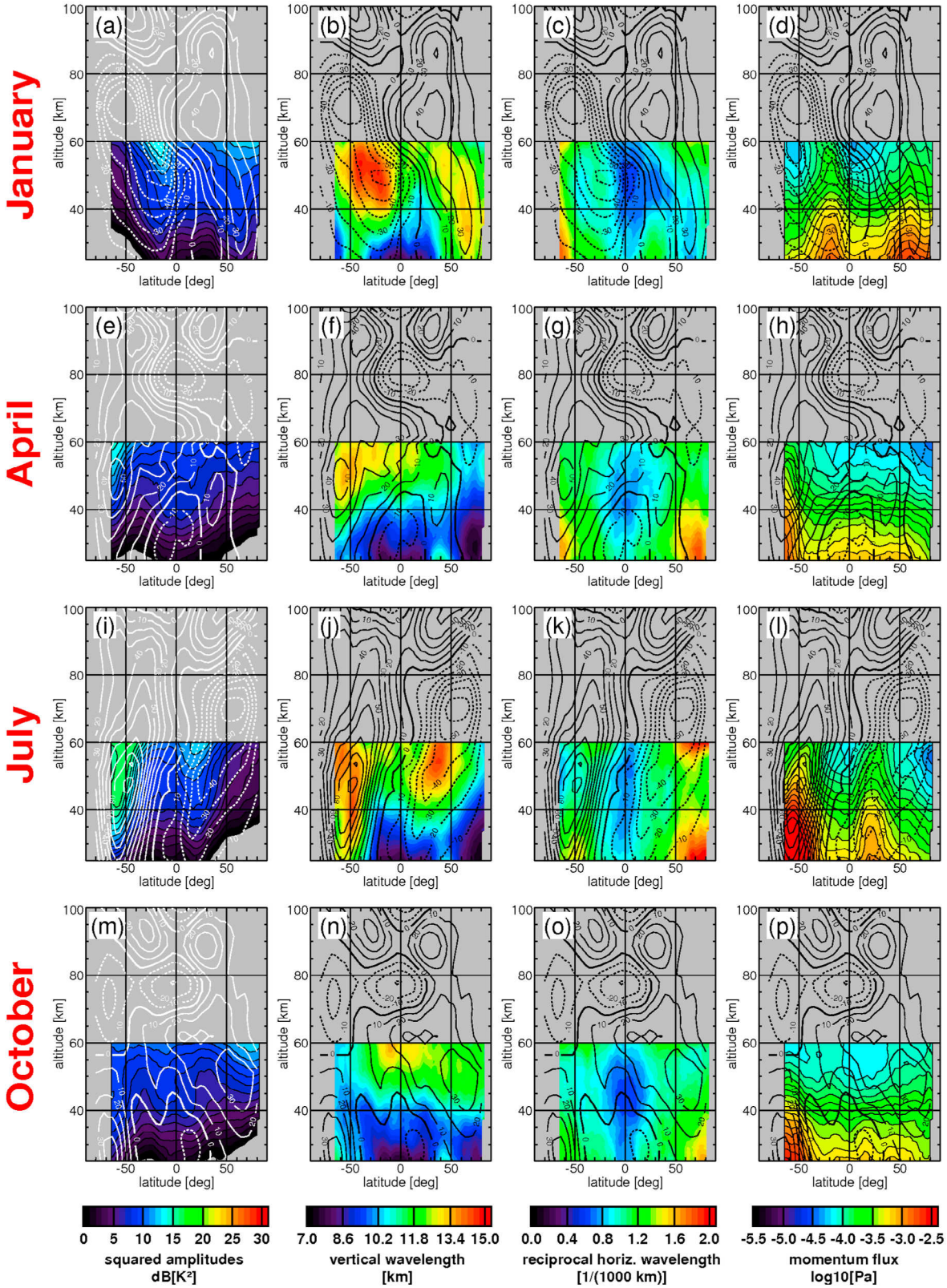

Figure 4. Zonal averages of HIRDLS gravity wave (a, e, i, and m) squared temperature amplitudes, (b, f, j, and n) vertical wavelengths, (c, g, k, and o) reciprocal horizontal wavelengths, and (d, h, l, and p) momentum flux absolute values for January (Figures 4a, 4b, 4c, and 4d), April (Figures 4e, 4f, 4g, and 4h), July (Figures 4i, 4j, 4k, and 4l), and October (Figures 4m, 4n, 4o, and 4p) 2006. In all panels contour lines of the SPARC zonal wind climatology are overplotted, contour increment is 10 m/s, dashed (solid) contour lines indicate westward (eastward) wind. For details see text.

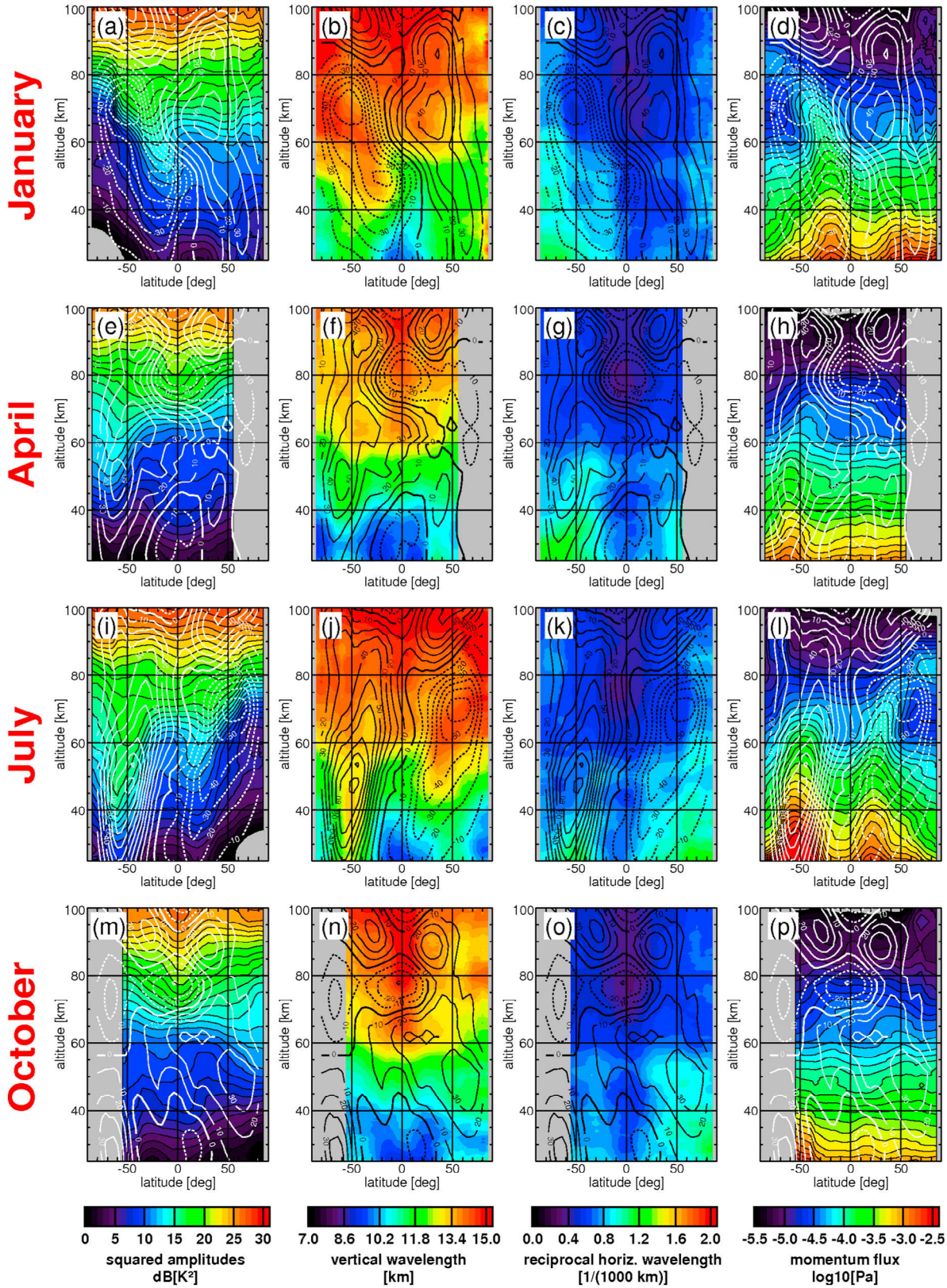

Figure 5. Same as Figure 4 but for the SABER instrument.

[73] The zonal cross sections shown in Figure 8 of *Yan et al.* [2010] cover the altitude range of about 22–55 km. This is about the same altitude range of HIRDLS data as in Figure 4 of our study. *Yan et al.* [2010] employ a different method for removing the atmospheric background state so that only GWs with horizontal wavelengths shorter than about 500–1000 km are discussed, i.e., only part of the GW spectrum seen by the satellite instrument. Therefore, only relative variations of GW amplitudes can be compared and not the absolute values.

5.2.1. Zonal Average Squared Temperature Amplitudes

[74] The first column in Figures 4 and 5 shows latitude-altitude cross sections of the zonal average GW squared temperature amplitudes obtained in our study for HIRDLS and SABER in January (Figures 4a and 5a), April (Figures 4e and 5e), July (Figure 4i and 5i), and October (Figure 4m and 5m) 2006. There is an overall good agreement between the squared amplitudes derived for HIRDLS and SABER. HIRDLS and SABER GW squared amplitudes agree within about one color level, which is about 30%.

[75] For all months a general increase of GW amplitudes with altitude is observed. This is as expected: GW amplitudes will grow exponentially with a scale height of about 14 km (twice the pressure scale height) if they propagate conservatively in a zero background wind atmosphere. This is simply an effect of energy conservation in an atmosphere with atmospheric density decreasing with height.

[76] Apart from this general behavior GW squared amplitudes are especially high in the strong zonal wind jets, in particular during January (Figures 4a and 5a) and July (Figures 4i and 5i). This increase of amplitudes is due to the fact that in non-zero background wind vertical propagation conditions are favorable for GWs propagating into opposite direction of the background wind, in particular, if there is also monotonic wind shear into the direction of the prevailing wind. The vertical wavelengths of those waves are Doppler-shifted toward longer values and, consequently, the amplitude threshold for the onset of GW breaking is enhanced [e.g., *Preusse et al.*, 2006, 2008].

[77] Another important feature in the summer hemisphere are the especially low GW amplitudes at high latitudes and the observed tilt of the global distribution from low latitudes toward the summer pole at high altitudes (above about 70 km). This tilt could indicate propagation of GWs from the subtropics toward higher latitudes in the summer hemisphere.

[78] There is an overall good agreement between the relative variations of the amplitude distributions in our study and the variations found by *Yan et al.* [2010]. Only the GW squared amplitudes obtained in our study are about twice as high because of the larger range of horizontal wavelengths covered.

[79] GW amplitude distributions for HIRDLS were also derived by *Alexander et al.* [2008] for May 2006 [cf. *Alexander et al.*, 2008, Figure 6]. Relative variations are similar to our results for April 2006 (Figure 4e). But the GW squared amplitudes obtained by *Alexander et al.* [2008] are also about a factor of two lower than our values. There can be several reasons for this difference: The study by *Alexander et al.* [2008] covers a smaller part of the GW spectrum (only vertical wavelengths shorter than 16 km). In addition, there are differences in the analysis techniques that will also contribute. For example, low covariance pairs of altitude profiles are included in *Alexander et al.* [2008], while altitude profiles that mismatch a vertical wavelength criterion are omitted in our study (see above). A more detailed comparison between our study and *Alexander et al.* [2008] is still an open issue.

5.2.2. Zonal Average Vertical Wavelengths

[80] The second column of Figures 4 and 5 shows latitude-altitude cross sections of the zonal average vertical wavelengths obtained in our study for HIRDLS and SABER in January (figures 4b and 5b), April (Figures 4f and 5f), July (Figures 4j and 5j), and October (Figures 4n and 5n) 2006.

[81] It should be noted that the HIRDLS instrument is sensitive to shorter vertical wavelengths because of the narrower vertical field of view. Therefore, SABER zonal average vertical wavelengths are generally somewhat higher in the stratosphere below about 40 km altitude. Apart from this general offset at low altitudes there is very good agreement between our HIRDLS and SABER values for all months.

[82] Similarly to *Yan et al.* [2010], we find enhanced vertical wavelengths especially in the strong zonal wind jets, as well as an overall increase of vertical wavelength with altitude. Our average vertical wavelengths are somewhat longer than the ones derived by *Yan et al.* [2010]. This difference could arise from the different methods used in our study and in that of *Yan et al.* [2010] or from the differences in the horizontal wavelength range covered (see above). On the other hand, there is very good agreement between our vertical wavelengths in April 2006 (Figure 4f) and the results obtained for May 2006 by *Alexander et al.* [2008].

[83] The general increase of vertical wavelengths with altitude is expected because GW amplitudes grow with altitude until saturation and, as short vertical wavelength waves saturate at lower altitudes, the GW spectrum at higher altitudes is more and more dominated by longer vertical wavelength waves [e.g., *Fritts and VanZandt*, 1993; *Gardner*, 1994].

[84] Increases of the vertical wavelengths with height at about 60 km altitude in the extratropics are likely not caused by an incomplete removal of global-scale tidal modes, because those increases are not closely correlated with strong increases in the horizontal wavelengths (see also the next subsection). Instead, those increases might be related to changes of the buoyancy frequency in the stratopause region.

[85] Latitudinal variations of the vertical wavelength distribution can be explained by Doppler shifting of the GW spectrum toward longer vertical wavelengths in the zonal wind jets. A more detailed discussion of the global variations of the GW vertical wavelength distribution is provided by, for example, *Ern et al.* [2006].

[86] As mentioned in *Ern et al.* [2006] the observed vertical wavelength distribution can also serve as a criterion to constrain the launch parameters of GWD parameterizations. The observed HIRDLS and SABER vertical wavelength distributions are very similar to the ones predicted by the *Warner and McIntyre* [2001] GWD parameterization used by *Ern et al.* [2006]. However more detailed studies are required.

5.2.3. Zonal Average Reciprocal Horizontal Wavelengths

[87] Distributions of the zonal average reciprocal horizontal wavelengths are given in the third column of Figures 4 and 5 for January (Figures 4c and 5c), April (Figures 4g and 5g), July (Figures 4k and 5k), and October (Figures 4o and 5o) 2006. As in work by *Ern et al.* [2004], horizontal wavelengths are longest around the equator. This means that the reciprocal wavelengths are especially low, indicating average horizontal wavelengths of 1000 km or longer. The equatorial maximum of horizontal wavelengths is related to the limitation of the GW frequency by the Coriolis parameter, which is more relaxed at the equator where the Coriolis parameter is zero. A more detailed discussion is given, for example, in section 3.3 of *Preusse et al.* [2006].

[88] Another striking feature is that reciprocal horizontal wavelengths in the winter polar jet are higher in the southern hemisphere in July 2006 than in the northern hemisphere during January 2006. This could hint at differences of the GW sources in the northern and southern winter jet. Maybe also the GW source processes in both hemispheres could be sensitive to the zonal wind speed. Zonal wind speed is much higher during July in the southern hemisphere, and this might lead to an excitation of shorter horizontal wavelength GWs.

[89] Reciprocal horizontal wavelengths for HIRDLS in April 2006 (Figure 4g) are somewhat higher than the ones derived by *Alexander et al.* [2008] for May 2006 [cf. *Alexander et al.*, 2008, Figure 6]. This could be an effect of the different methods used to remove the global scale atmospheric background. Further reasons could be the different methods used for the vertical analysis of altitude profiles or the differences in the vertical wavelength ranges of both studies (see above). The relative distributions are however very similar.

[90] Horizontal wavelengths determined from SABER data are somewhat longer than HIRDLS values. This is likely an effect of the longer SABER horizontal sampling distances along the measurement track. This causes an undersampling of waves with very short horizontal wavelengths and, consequently, results in a greater overestimation of the horizontal wavelengths on average. This effect has also been observed for CRISTA [*Ern et al.*, 2004] and was accounted for by an aliasing correction. No corrections are applied to HIRDLS and SABER data.

[91] It should also be mentioned that for SABER an overall decrease of reciprocal horizontal wavelengths with altitude (i.e., an increase of horizontal wavelengths) is observed. This is partly due to larger aliasing as the sampling distance of SABER increases with altitude (see also Figure 1). However, decreases of the reciprocal horizontal wavelength observed by HIRDLS are reliable below 50 km altitude (above 50 km the noise increases) and indicate longer horizontal wavelengths due to physical reasons.

[92] There are further features of the horizontal wavelength distribution that are not fully understood, for example the increase of reciprocal horizontal wavelengths around 50 km altitude seen in the SABER data. In addition, there is a drop of reciprocal horizontal wavelengths around the equator at altitudes above about 70 km. This drop is accompanied by narrow tropical maxima of the GW squared amplitudes and vertical wavelengths and is likely due to diurnal tides, which exhibit a local maximum there, and are not fully removed at low latitudes and high altitudes. Therefore, derived GW parameters will be subject to larger errors in this region.

5.2.4. Zonal Average Gravity Wave Momentum Fluxes

[93] Finally, in the fourth column of Figures 4 and 5 HIRDLS and SABER zonal average distributions of GW momentum fluxes are given for January (Figures 4d and 5d), April (Figures 4h and 5h), July (Figures 4l and 5l), and October (Figures 4p and 5p) 2006.

[94] If GWs propagate conservatively, it is expected that GW momentum flux should be constant with increasing altitude. Instead, a general decrease of GW momentum flux with altitude is observed, indicating that dissipation of GWs takes place in the whole altitude range.

[95] Apart from this general behavior especially high values of GW momentum flux are found in the polar jets of the winter hemisphere during January and July (see Figures 4d, 4l, 5d, and 5l). GW momentum flux in the southern winter polar jet is considerably higher than in the northern winter polar jet (about twice as high). High values of GW momentum flux are also found in the subtropics of the summer hemisphere. Those enhanced values are caused by GWs generated by deep convection in the monsoon regions. For comparison, see also the horizontal distributions of GW momentum flux shown in Figure 3. It should also be noted that the GW momentum flux in the polar jets decreases stronger with altitude than the GW momentum flux in the subtropics. Therefore, at 70 km altitude the momentum flux in the subtropics in the summer hemisphere is stronger than that of the GWs in the polar jet.

[96] The GW momentum flux distribution around equinox (Figures 4h, 4p, 5h, and 5p) shows only little latitudinal structure. In April GWs in the southern polar jet and mountain waves above South America and the Antarctic Peninsula still cause some enhancement, however in October there is almost no dominant latitudinal structure left.

[97] The HIRDLS zonal average distribution of GW momentum flux for April 2006 (Figure 4h) should be similar to the one obtained by *Alexander et al.* [2008] for May 2006, also from HIRDLS data. Indeed, the relative distribution of GW momentum flux is very similar. But, like for the GW squared amplitudes, the values obtained in our study are considerably higher (about a factor of two). As mentioned above, possible reasons could be the smaller vertical wavelength range covered by *Alexander et al.* [2008] or differences in the analysis techniques between our study and that of *Alexander et al.* [2008].

[98] HIRDLS and SABER momentum fluxes in our study are in an overall agreement, both in the general distribution, as well as in absolute numbers. The good quantitative agreement, however, is partly a result of a compensation of larger horizontal wavelengths (smaller wavenumbers) by larger temperature squared amplitudes observed by SABER in comparison to HIRDLS. For SABER on average longer GW horizontal wavelengths are expected, because of the larger profile distances and hence longer horizontal wavelength Nyquist limit. Differences in the GW amplitudes seen in different infrared limb sounders might depend on details of the temperature retrieval process and can be estimated only by dedicated simulations [e.g., *Preusse et al.*, 2002; *Ungermann et al.*, 2010]. In particular, the different orbit and viewing geometry may contribute. Resulting effects on

GW momentum fluxes are however less than 30% and therefore well inside our error estimates (see also section 4).

[99] One important feature that is already indicated in the zonal average distributions of GW squared amplitudes becomes now even more obvious in the GW momentum flux distribution: especially in January and July the GW momentum flux maximum in the summer hemisphere shifts more and more poleward with increasing altitude (see Figures 5d, and 5l). This poleward shift is in good agreement with GW ray-tracing simulations by, for example, *Preusse et al.* [2009b] or *Sato et al.* [2009]. These studies both indicate a poleward propagation of GWs of about 15° between 30 and 70 km altitude caused by refraction of GWs into the strong zonal wind jets of the summer mesosphere.

[100] Further indication that this effect seen in the momentum flux distributions is indeed an observed latitudinal shift of GWs are the local increases of GW momentum flux with altitude poleward of 40° latitude above 60 km altitude in the summer hemisphere (see Figures 5d, and 5l). This likely cannot be explained by purely vertical propagation of GWs alone.

[101] A second effect which could contribute is Doppler shifting of the GW spectrum in strong wind shear so that satellite instruments see different parts of the GW spectrum at different altitudes because of their observational filter. However, for limb sounders this effect is likely not important in the mesosphere [*Preusse et al.*, 2006]. This is further supported by the fact that the summertime momentum flux maxima follow the strongest wind gradient and are not closely related to the absolute wind speed.

[102] Characteristic for GWs generated by deep convection in the monsoon regions are their particularly short horizontal wavelengths. In global distributions of GW horizontal wavelengths (not shown) these regions of short horizontal wavelengths are latitudinally shifted with altitude, which is a further indication for the poleward propagation of GWs generated by deep convection in the subtropics into the easterly summer jet.

[103] This means that there is strong evidence for nonvertical propagation of GWs generated by deep convection in the monsoon regions of the summer hemisphere. Those GWs likely contribute significantly to the wind reversal at higher latitudes, as well as to the poleward tilt of the summertime mesospheric jets.

[104] In the stratosphere latitudinal shifts between the observed subtropical summertime maxima of GW activity at around 38 km altitude and the corresponding locations of the source regions, i.e., the monsoon regions in the troposphere, have also been found before in UARS-MLS data by *Jiang et al.* [2004b]. However, these observations strongly suffer from the only very small part of the GW spectrum that is observed. In addition, the results provide no clear picture in the mesosphere.

[105] Above altitudes of 70–80 km tides become the dominating global-scale wave modes. Since tides are at the edge of or outside the properly resolved frequency range of our space-time spectra, SABER GW momentum fluxes potentially become less reliable. In particular, at high altitudes in the tropics the latitude-altitude structure of the diurnal migrating tide (DW1) [e.g., *Forbes et al.*, 2006; *Mukhtarov et al.*, 2009] is resembled by a pattern of longer horizontal GW wavelengths (smaller values in Figure 5, third column). This indicates that the DW1 tide in this region cannot be fully removed by our approach based on 31-day average tidal amplitudes. Above 90 km also other tidal modes that are neglected in our atmospheric background removal can attain large amplitudes [e.g., *Forbes et al.*, 2006; *Pancheva et al.*, 2010]. These modes, however, have vertical wavelengths considerably longer than the maximum vertical wavelength of 25 km considered in our analysis, in addition, horizontal wavelengths at higher latitudes remain short at high altitudes (no decreased values in Figure 5, third column). Still, above 90 km altitude SABER GW momentum flux values are considered less reliable (see also section 3.1.2).

[106] Another feature of the momentum flux distribution that is not understood are the enhanced values of GW momentum flux in January and July in the summer hemisphere poleward of about 60° latitude, between about 80 and 90 km altitude (see Figures 5d and 5l). These regions coincide with regions of high reciprocal horizontal wavelengths in Figures 5c and 5k, indicating larger vertical phase shifts on average, i.e., low correlation between neighbored pairs of altitude profiles. This could be a real effect, but this could also hint at problems in removing the global-scale background or problems of the temperature retrieval around the cold summer mesopause. Also in the stratopause region the increase of reciprocal horizontal wavelengths mentioned in section 5.2.3 is not understood and might be an indication of less reliable momentum fluxes.

5.2.5. Zonal Average Potential Accelerations Due to Gravity Waves

[107] To find out where interactions between GWs and background wind are strongest, similar as in equation (2), we now calculate estimates for the accelerations XY_{pot} that can be expected from vertical gradients in the absolute values of GW momentum flux F_{ph}:

$$XY_{pot} = -\frac{1}{\rho}\frac{\partial F_{ph}}{\partial z}. \quad (5)$$

[108] We call these values "potential acceleration" because they are only very rough estimates and there are several caveats that have to be kept in mind:

[109] 1. Only part of the GW spectrum is observed by the HIRDLS and SABER instruments and therefore only part of the accelerations.

[110] 2. Doppler shifting of the GW vertical wavenumber spectrum will move parts of the GW spectrum in and out of the visibility range of the instruments. This sometimes might bias the potential accelerations. (However, wave saturation is likely the dominant process that shapes the observed global distributions of GW activity [*Preusse et al.*, 2006].)

[111] 3. No corrections for undersampling and instrument sensitivity to GWs have been applied and GW momentum fluxes will therefore be low-biased (see section 4). This will result in further errors of the potential accelerations.

[112] 4. Our GW momentum fluxes are only absolute values, and the propagation direction of the single waves is not known. Therefore, also the direction of the accelerations is not known and only positive values are given.

[113] 5. Because momentum flux of different waves could cancel out, true accelerations could be even zero although non-zero potential accelerations are calculated.

[114] 6. Potential accelerations are calculated via equation (5). This equation is only valid for purely vertical propagation of GWs. In case of non-vertical propagation equation (5) does not hold and a more general expression has to be used [e.g., *Preusse et al.*, 2009b]. In particular, negative potential accelerations arising from local vertical increases of GW momentum flux are not meaningful.

[115] Despite all these caveats potential accelerations will provide valuable information. Especially in strong wind jets the GW spectrum has significant anisotropies caused by wind filtering of the GW spectrum [e.g., *Warner et al.*, 2005; *Gong et al.*, 2008]. GWs propagating against the prevailing wind have more favorable propagation conditions and will dominate the momentum fluxes observed. If these waves dissipate this will be the dominant effect responsible for observed momentum flux vertical gradients. Therefore, especially in and directly above the strong zonal wind jets potential accelerations will give a rough estimate of the "real" accelerations and, at least, indicate where effects on the background wind by GW dissipation can be expected.

[116] The zonal wind jets in stratosphere and mesosphere are strongest in January and July. Therefore, we focus on these two months because accelerations of the zonal winds by GWs will be most significant. The potential accelerations calculated for January and July 2006 are given in Figure 6 in m/s/day on a logarithmic scale for HIRDLS (Figures 6a and 6b) and SABER (Figures 6c and 6d). Regions not covered with data and values below 0.1 m/s/day are masked with light grey color. Again, like in Figures 4 and 5, for comparison zonal winds of the SPARC climatology are also given as contour lines.

[117] To maintain the climatological state in the mesosphere absolute values of total net GWD (i.e., net values of orographic plus nonorographic GWD) in GCMs in January and July usually display maxima around 80 km altitude. Peak values are between about 20 and 100 m/s/day. They vary from model to model and are also different in different hemispheres [e.g., *Manzini and McFarlane*, 1998; *Mieth et al.*, 2004; *Watanabe et al.*, 2008; *Richter et al.*, 2010; *Orr et al.*, 2010]. This shows the large uncertainty inherent in the momentum budget of the mesosphere to obtain the desired circulation pattern.

[118] Values of potential accelerations obtained around 80 km altitude in our study are between about 10 and 20 m/s/day, i.e. considerably lower, at least by a factor of two. Only in the summer hemisphere somewhat higher values are found (see Figure 6). One possible reason for those significantly lower values could be, for example, that only part of the GW spectrum (only horizontal wavelengths >100–200 km and vertical wavelengths in the range 2–25 km), and therefore only part of the GWD, is covered by our analysis. In the mesopause region, however, also GWs might become important that have longer vertical and/or shorter horizontal wavelengths. Another reason could be that SABER and HIRDLS momentum fluxes are not corrected for horizontal undersampling of waves and for effects of the observational filter, and therefore are likely low-biased (see also section 4).

[119] In the stratosphere absolute values of total net GWD in GCMs are usually much lower and do not exceed values of about 1 m/s/day [e.g., *Mieth et al.*, 2004; *Watanabe et al.*, 2008; *Orr et al.*, 2010]. Only in the study by *Richter et al.* [2010] peak values in January are about 1–2 m/s/day, but only in the northern hemisphere. Values for July are not shown by *Richter et al.* [2010].

[120] In our study potential accelerations observed in the wintertime polar jet in the northern hemisphere during January are also about 1–2 m/s/day (see Figures 6a and 6c), i.e., in good agreement with the values by *Richter et al.* [2010]. Potential accelerations of about 1–2 m/s/day in the subtropics of the summer hemisphere between about 35 and 50 km altitude in both January and July are however higher than values obtained in GCMs.

[121] The largest discrepancy to GWD obtained in GCMs is found in the wintertime polar jet during July. Potential accelerations are about 5–10 m/s/day around 50°S (see Figures 6b and 6d), and it is remarkable that these significant accelerations due to GWs are found already in the stratosphere. Peak values can even be somewhat higher.

[122] These values exceed typical stratospheric values of GWD obtained in GCMs by at least a factor of three (see above), and this large discrepancy is still not understood. One possible reason could be the strong intermittency of GW amplitudes and momentum fluxes observed in the real atmosphere [e.g., *Hertzog et al.*, 2008]. In the overall distribution of GWs in a given region there will sometimes be GWs with exceptionally high amplitudes that could saturate already in the stratosphere. This could result in enhanced values of GWD at altitudes lower than expected from nonorographic GWD schemes in GCMs with their uniform and constant source distributions that do not account for this effect. Another reason for those enhanced potential accelerations could be aspects of GW propagation that are not fully understood. For example, back-reflection of GWs in the stratosphere could cause vertical gradients of momentum fluxes without affecting the zonal mean flow.

[123] It should be noted that high values of GWD in the stratosphere of about 5 m/s/day in the polar night jets have also been estimated from the momentum budget of the ERA-40 reanalysis [*Monier and Weare*, 2011]. Of course, also those values will be subject to large errors, however this shows the large uncertainties that still exist in the overall momentum budget at high latitudes.

[124] The significant potential accelerations in the stratosphere found in our study could be a hint that the effect of GWs in the stratosphere is still underestimated in GCMs. This is an important finding because it has been shown in GCM studies by *Sigmond et al.* [2008] that the downward coupling between stratosphere and troposphere at mid and high latitudes and, consequently, the tropospheric response to climate change is very sensitive to parameterized GWD. This means that missing effects like the enhanced GWD already at low altitudes in the polar night jets have to be included in GCMs to improve their predictive capabilities in a changing climate, in particular for regional scales.

[125] Another important finding from Figure 6 are high accelerations in the summer hemisphere above about 50 km altitude between 20 and 50° latitude, in a region tilted poleward with altitude. It is likely that GWs that are excited in the monsoon regions and that have shifted poleward with altitude contribute to those accelerations (see also the GW momentum flux distributions discussed in section 5.2.4).

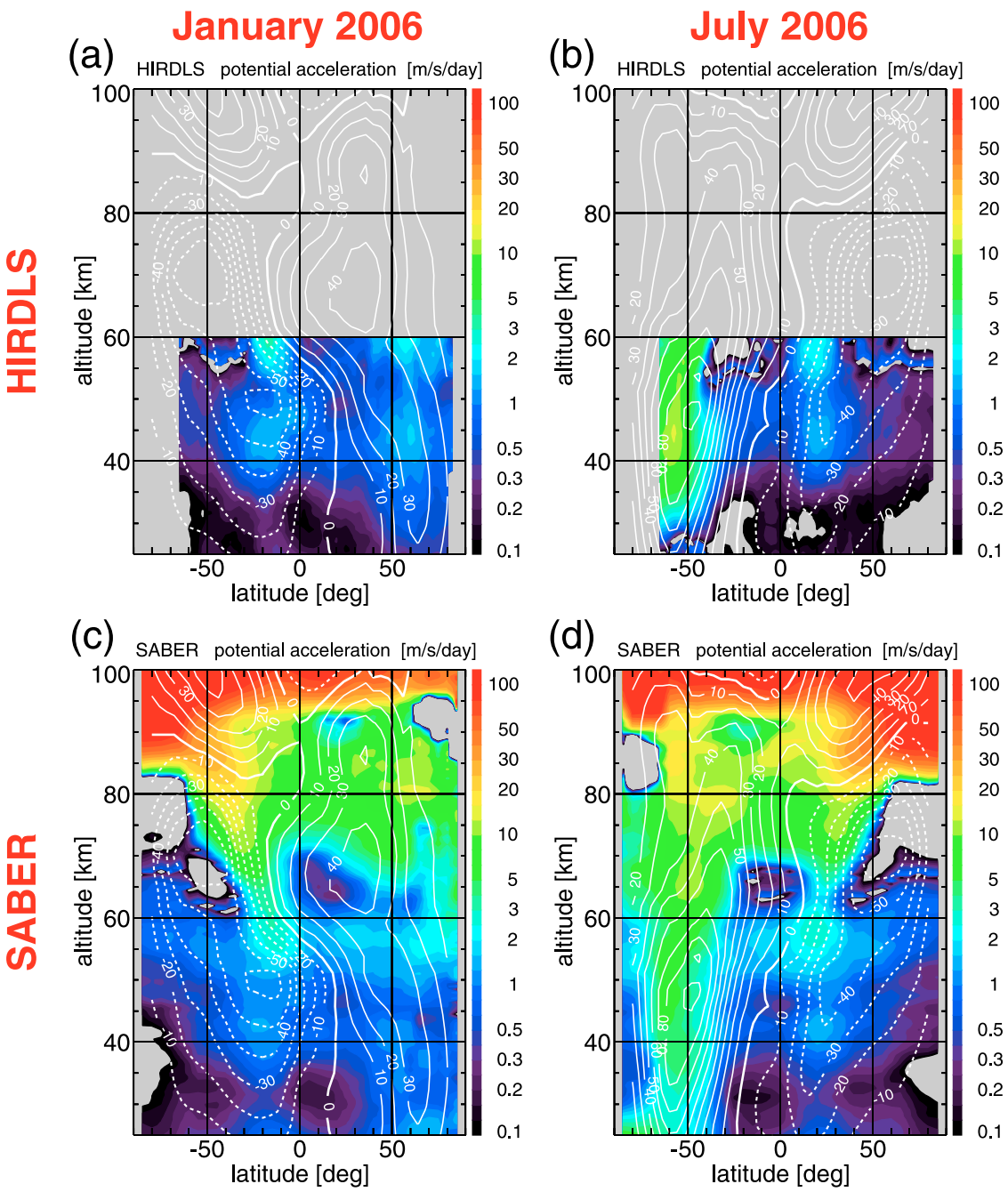

Figure 6. Potential accelerations (absolute values) for the part of the gravity wave spectrum seen by (a and b) HIRDLS and (c and d) SABER for January 2006 (Figures 6a and 6c), and July 2006 (Figures 6b and 6d). Accelerations are smoothed vertically with a 5 km running mean and values are given in m/s/day on a logarithmic color scale. In all panels contour lines of the SPARC zonal wind climatology are overplotted, contour increment is 10 m/s, dashed (solid) contour lines indicate westward (eastward) wind. For details see text.

This means that these GWs will contribute to the overall momentum budget exactly where a poleward tilt of the mesospheric summer jet is observed, and could indicate that cross-latitude propagation of GWs might play an important role in this region.

[126] Like the momentum flux distributions, also potential accelerations will be less reliable at altitudes above about 80 km (see also the discussion in section 5.2.4). Nevertheless, the further increase of potential accelerations toward higher altitudes indicates that at higher altitudes the effect of GWs on the background winds is even more important.

6. Seasonal and Longer-Term Variations in Stratosphere and Mesosphere Observed in Nine Years of SABER Data

[127] The SABER data set is now almost nine years long and measurements are still ongoing. Therefore, this data set

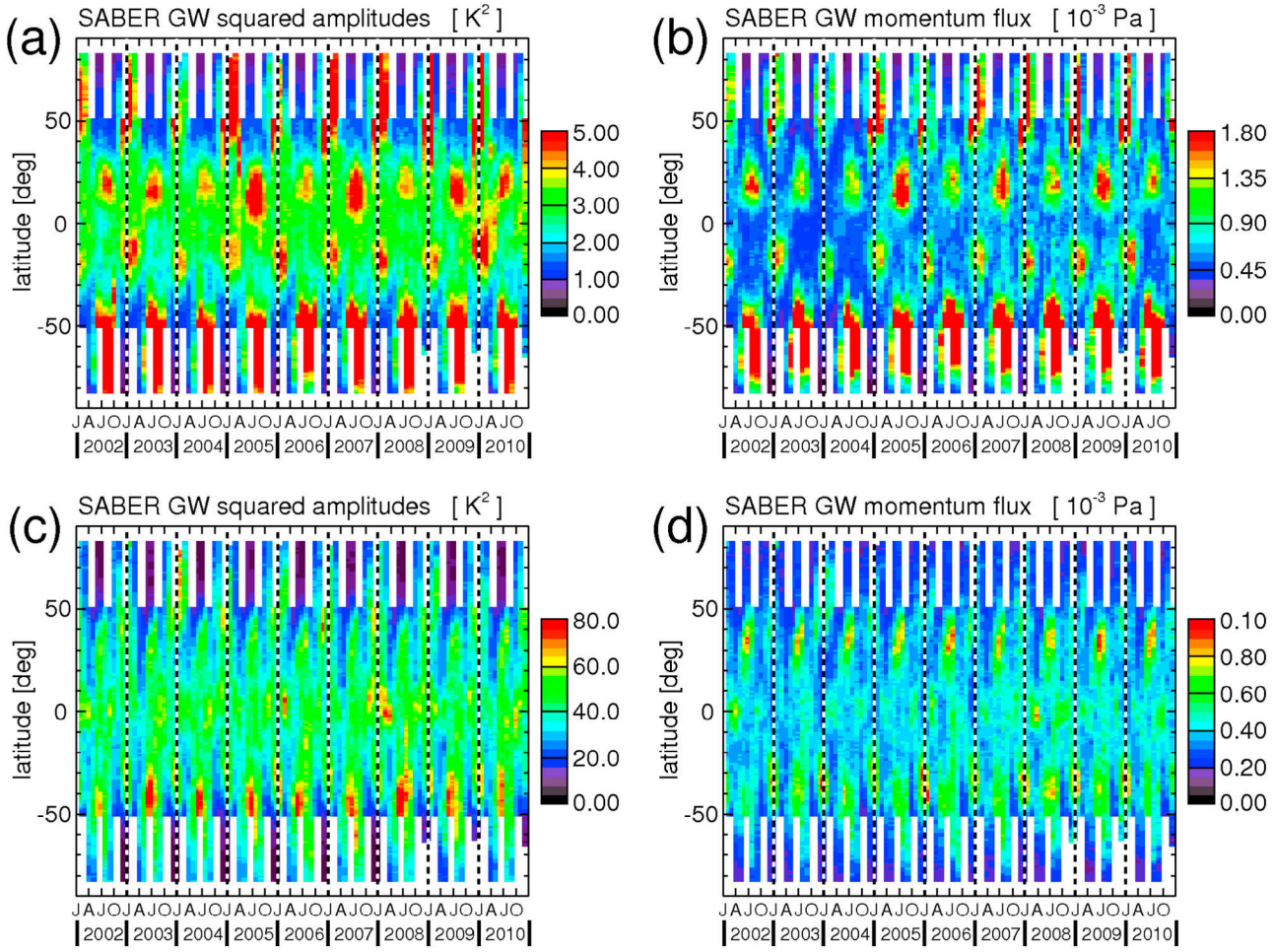

Figure 7. Latitude-time cross section of SABER gravity wave (a) squared temperature amplitudes at 30 km altitude, (b) momentum flux absolute values at 30 km altitude, (c) squared temperature amplitudes at 70 km altitude, and (d) momentum flux absolute values at 70 km altitude. Squared amplitudes are given in K^2, momentum fluxes in 10^{-3} Pa. For details see text.

is well suited to investigate seasonal and longer-term variations of GW parameters in the stratosphere and mesosphere up to time scales of the 11-year solar cycle.

[128] Figure 7 shows latitude-time cross sections of SABER zonal mean GW squared temperature amplitudes (Figures 7a and 7c) and GW momentum fluxes (Figures 7b and 7d) at 30 km (Figures 7a and 7b) and 70 km (Figures 7c and 7d) altitude. The temporal resolution of the time series is 31 days. The 31-day zonal averages are synchronized with the SABER yaw cycles to avoid averaging across the days of the yaw maneuvers and to clearly separate northward and southward viewing geometries.

6.1. Seasonal and Longer-Term Variations in the Stratosphere

6.1.1. Seasonal Variations

[129] Figure 7a is a latitude-time cross section of SABER zonal mean GW squared temperature amplitudes in K^2 at 30 km altitude. As already seen in the vertical cross sections of GW squared amplitudes shown in Figures 4 and 5 it is also evident from Figure 7a that the main source for enhanced GW squared amplitudes are indeed the polar vortices in the winter hemisphere and the convectively generated GWs over the monsoon regions, centered at about 20° latitude in the summer hemisphere. On zonal average, only little wave activity is found at high latitudes in the summer hemisphere and in the subtropics of the winter hemisphere.

[130] These variations are also seen in the latitude-time cross section of GW momentum fluxes at 30 km altitude shown in Figure 7b. In the momentum fluxes the variation in the subtropics is even more pronounced because horizontal wavelengths are especially short for the GWs that are generated by strong convection in the monsoon regions [e.g., *Ern et al.*, 2004; *Alexander et al.*, 2008], leading to an enhanced contrast between high and low values of GW momentum flux.

[131] Comparison of GW squared amplitudes in the stratosphere (Figure 7a) with the climatology of GW potential energies by *Tsuda et al.* [2000], derived from GPS radio occultations, shows about the same relative structures: High GW activity on the winter hemisphere in the polar night jets and very low GW activity in the summer hemisphere high latitudes. The main difference are the high values of potential energies in the tropics seen by *Tsuda et al.* [2000], which are not present in our study. Likely explanations are

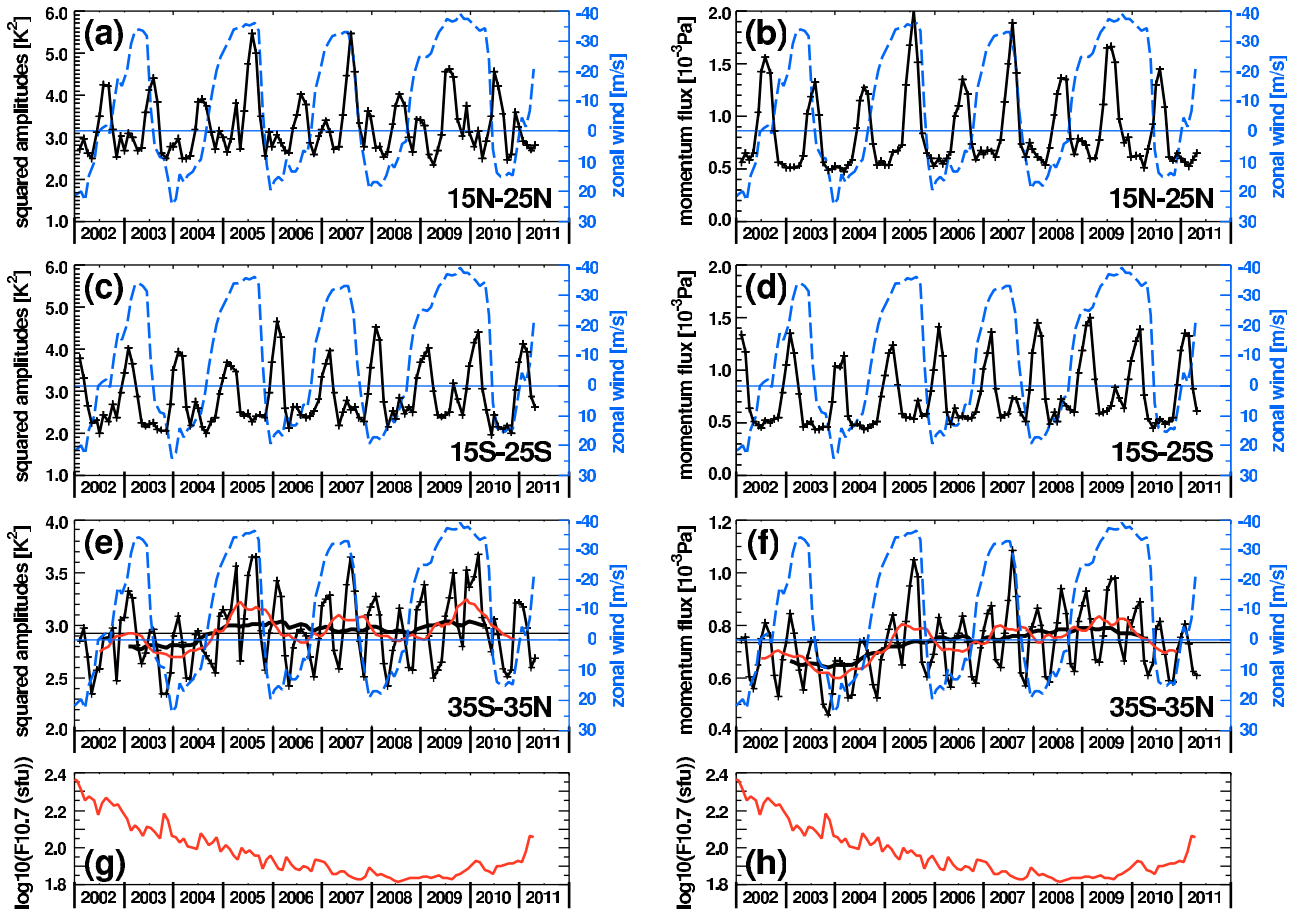

Figure 8. Time series of (a, c, and e) SABER gravity wave squared amplitudes and (b, d, and f) gravity wave momentum flux absolute values at 30 km altitude (black solid lines marked with crosses). Values are averaged over the latitude bands: 15°N–25°N (Figures 8a and 8b), 15°S–25°S (Figures 8c and 8d), and 35°S–35°N (Figures 8e and 8f). In Figures 8e and 8f also 13-month running means (red lines) are given to highlight the overall QBO variation of gravity wave activity in the latitude band 35°S–35°N. Also given in Figures 8a–8f are equatorial zonal winds (m/s) observed at Singapore (1°N, 104°E) at the 15 mbar pressure level, i.e. about 30 km altitude (blue dashed lines). Please note that the y-scale on the right is reversed for better comparison. To highlight longer-term variations in the latitude band 35°S–35°N also 25-month running means (thick black lines) and the median (horizontal black line) of the GW squared amplitudes and momentum fluxes are given in Figures 8e and 8f. g and h) For comparison, monthly values of the 10.7 cm solar flux on a logarithmic scale are shown.

remnants of short vertical-wavelength Kelvin waves (i.e., global-scale waves) not removed from the GPS data by merely vertical filtering of altitude profiles, and the different vertical wavelength ranges considered.

6.1.2. Possible Effects of the QBO

[132] In Figures 7a and 7b a clear quasi-biennial variation of the subtropical GW maxima can be seen, especially in the northern hemisphere. Possible reasons are QBO modulation of the deep convection in the monsoon regions [e.g., *Mohankumar and Pillai*, 2008; *Giorgetta et al.*, 1999], QBO related variations of the wind filtering of GWs between their source level and 30 km altitude, some minor effects of the instrumental observational filter caused by QBO induced variations in the Doppler shifting of the observed waves, or a combination of all those effects. This quasi-biennial variation of GWs in the subtropics has already been found before in SABER GW variances [*Krebsbach and Preusse*, 2007].

[133] Interannual variation of GW squared amplitudes and momentum fluxes in the wintertime polar vortices can also be found in Figures 7a and 7b. Part of the observed variation in the northern hemisphere is likely connected with stratospheric warmings as has been shown, for example, by *Wang and Alexander* [2009] or *Wright et al.* [2010].

[134] The QBO-related variations of GW activity in the subtropics and tropics are further illustrated in Figure 8. Shown are the time series of SABER GW squared amplitudes (Figures 8a, 8c, and 8e) and GW momentum flux absolute values (Figures 8b, 8d, and 8f) at 30 km altitude (black solid lines marked with crosses). The values are averaged over the latitude bands 15°N–25°N (Figures 8a and 8b), 15°S–25°S (Figures 8c and 8d), and 35°S–35°N (Figures 8e and 8f). Also given in Figures 8a–8f are equatorial zonal winds in m/s (blue dashed lines) observed at Singapore (1°N, 104°E) at the 15 mbar pressure level, i.e. at about the same altitude as the observations. Please note that

the zonal wind scale given on the right y-axis in Figures 8a–8f is reversed for better comparison.

[135] In the latitude band 15°N–25°N we find clear indication of enhanced subtropical GW activity in summer during phases of QBO westward wind. A possible explanation could be that the zonal wind in the upper troposphere is also westward in summer, so that GWs do not encounter a wind reversal and vertical propagation conditions are more favorable than during phases of QBO eastward wind. Still, we find strong interannual variability that might also indicate influences of GW source variations.

[136] In the latitude band 15°S–25°S also biennial variations are visible, however there is no such clear relationship between GW activity and the QBO winds at the same altitude. This might indicate that also variations in the GW sources might be important, or that the influence of the QBO is weaker in the subtropics on the southern hemisphere.

[137] In the wider latitude band 35°S–35°N, including both tropics and subtropics, there is an even better correlation between GW activity and the QBO winds at the same altitude (see Figures 8e and 8f). In Figures 8e and 8f also 13-month running means (red lines) of GW squared amplitudes and GW momentum fluxes are given to highlight the good coincidence of high GW activity and QBO westward winds.

6.1.3. Long-Term Variations on Time Scales of the 11-Year Solar Cycle

[138] Another striking feature is an overall long-term variation of GW momentum flux at 30 km altitude with low values in 2002/2003, an increase toward the years 2008/2009, and again a decrease starting in 2009. This variation can most clearly be seen in the background momentum flux values, away from the seasonal maxima in the summertime subtropics and the polar night jets (see Figure 7b). This variation is also highlighted by a 25-month running mean (bold black solid lines) of the GW squared amplitudes and momentum fluxes averaged over the latitude band 35°S–35°N (see Figures 7e and 7f). In the momentum fluxes the observed variation is more obvious because also GW vertical and horizontal wavelengths exhibit long-term variations, increasing the observed effect. On average, toward the years 2008/2009 GW vertical wavelengths are somewhat longer and horizontal wavelengths shorter (not shown). There are no indications that variations of instrument noise could be a possible reason for all those observed long-term variations.

[139] Comparison of GW amplitudes and momentum fluxes (Figures 7e and 7f) with the 10.7 cm solar flux on a logarithmic scale (Figures 7g and 7h) might indicate an anti-correlation between the 11-year solar cycle and GW activity. But, of course, a 9-year data set is much too short for this kind of study. In particular, also other decadal variations in the whole Earth system, not directly related to the 11-year solar cycle, could be a possible explanation for the observed variations.

[140] Nevertheless, long-term variations of GW activity are still an open issue in atmospheric dynamics. Observations from single measurement stations sometimes indicate positive and sometimes negative correlation of GW activity with long-term changes of solar activity, and some of the longer-term variations are also attributed to changes in the local meteorological conditions [e.g., *Gavrilov et al.*, 1995, 2002, 2004; *Jacobi et al.*, 2006b]. This means that obviously an overall global picture is still missing, which shows the importance of further SABER observations in the forthcoming years.

6.2. Seasonal and Longer-Term Variations in the Mesosphere

[141] Figure 7c shows a latitude-time cross section of SABER GW squared amplitudes at 70 km altitude in K^2. As already mentioned in section 5.2.4 the subtropical GW maxima have undergone a poleward shift by about 15° in latitude between 30 and 70 km altitude, leading to a semi-annual cycle in GW squared amplitudes in parts of the northern and southern hemisphere. This poleward shift is in excellent agreement with GW ray-tracing simulations showing that GWs generated in the subtropics are refracted toward higher latitudes [e.g., *Preusse et al.*, 2009b; *Sato et al.*, 2009]. Even the magnitude of the observed poleward shift can be reproduced and is about the same for all years covered by our study. This underlines the importance of GWs generated in the subtropics for GW variances observed in the middle and upper mesosphere at midlatitudes.

[142] Observations indicate that GWs can also be generated by strong convection at midlatitudes [*Hoffmann and Alexander*, 2010] and will likely reach the mesosphere. The relative importance of those waves has however not been studied so far.

[143] For comparison with the GW squared amplitudes Figure 7d shows the corresponding SABER latitude-time cross section of GW momentum fluxes. Strikingly, different from the GW squared amplitudes, momentum fluxes show rather an annual than a semi-annual variation in the northern hemisphere. In the southern hemisphere the semiannual variation of the GW squared amplitudes is dominated by the wintertime maximum, while in GW momentum fluxes the summertime maximum is higher between about 20°S and 40°S.

[144] This means that in the global GW momentum flux distribution at 70 km the GW momentum fluxes in the wintertime polar regions no longer are the dominant features. Obviously, the GWs that are still very prominent in the stratospheric polar night jet deposit a considerable amount of their momentum already in the stratosphere and lower mesosphere (see also sections 5.2.4 and 5.2.5). Therefore, in the mesosphere above about 70 km altitude the summertime momentum flux maxima that can be attributed to GWs generated in the subtropical monsoon regions are much higher.

[145] Another finding is that in the southern hemisphere the wintertime maxima of GW squared amplitudes and momentum fluxes have shifted considerably equatorward, corresponding to the equatorward tilt of the southern polar night jet in the mesosphere (see also sections 5.2.1 and 5.2.4). This tilt is obviously a persistent feature over the whole nine-year period covered by SABER data. This effect can also be seen in the northern hemisphere, however during winter in the northern hemisphere GW squared amplitudes and momentum fluxes are more dominated by enhancements that are likely connected with major stratospheric warmings [see also *Hoffmann et al.*, 2007; *Manney et al.*, 2008]. This is the case especially in the winters 2003/2004, 2005/2006, 2007/2008, and 2008/2009.

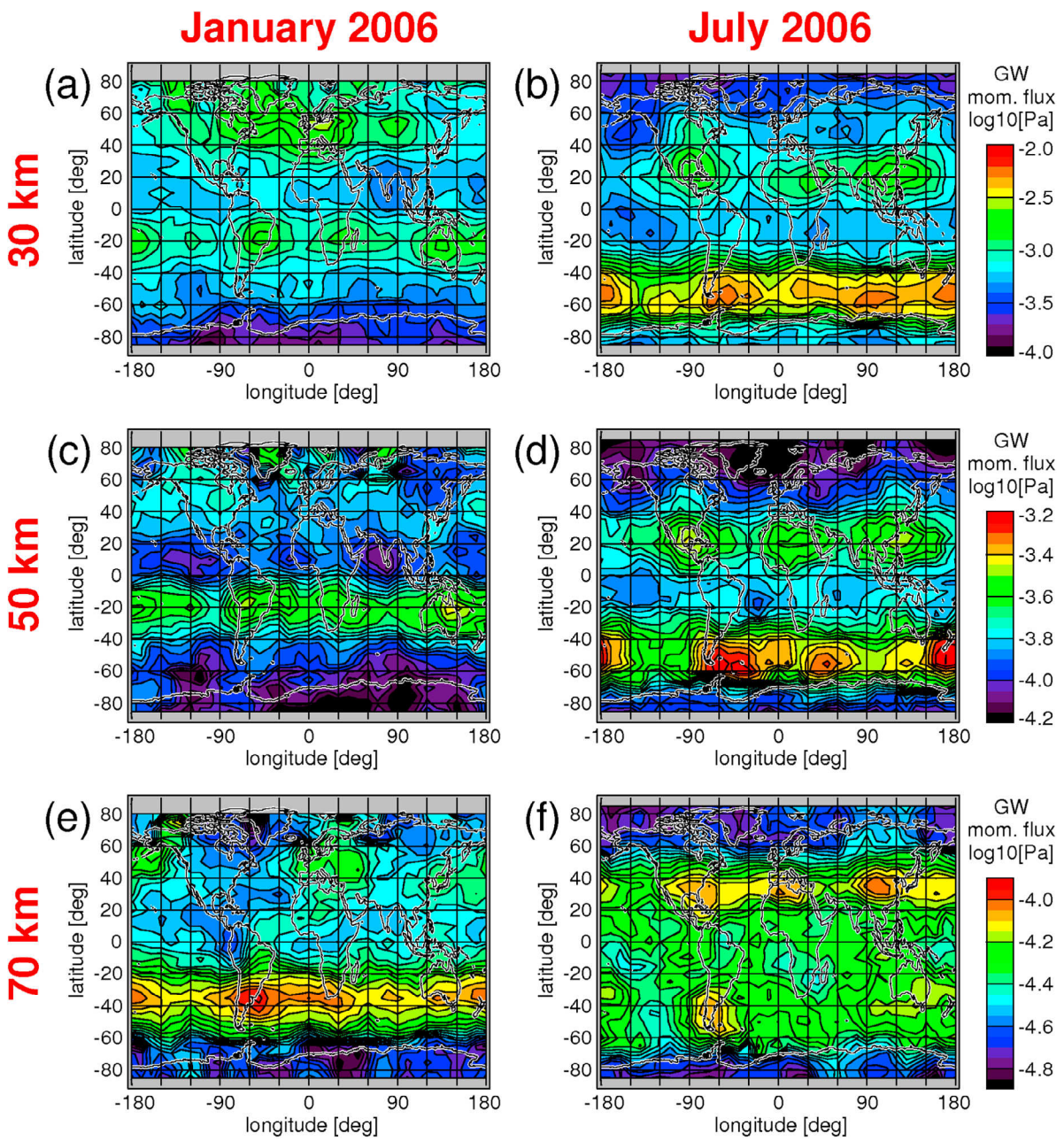

Figure 9. Average horizontal distribution of SABER gravity wave momentum flux absolute values for (a, c, and e) January and (b, d, and f) July 2006 at the altitudes 30 km (Figures 9a and 9b), 50 km (Figures 9c and 9d), and 70 km (Figures 9e and 9f). Values are given in $\log_{10}$ (Pa). The same color scale is used for both panels in a row, i.e., for both January and July at the same altitude. For details see text.

[146] Long-term variations that might be due to the 11-year solar cycle can also be seen in the GW squared amplitudes and momentum fluxes observed in the mesosphere, but the effect seems to be weaker than in the stratosphere. Also the QBO modulation of the summertime GW momentum flux maxima is not as obvious as in the stratosphere (see Figures 7c and 7d).

[147] Finally, it should be noted that at 70 km altitude squared amplitudes are enhanced at the equator. This feature is likely a bias caused by not fully removed tides at low latitudes and higher altitudes (see also sections 5.2.3 and 5.2.4). This equatorial maximum is less enhanced in the momentum fluxes since the tidal remnants have very long horizontal wavelengths.

7. Variation of the Horizontal Distribution of Gravity Wave Momentum Flux With Altitude

7.1. Observed Variations

[148] In the following, changes of the horizontal distribution of GW momentum flux with altitude are investigated. Figure 9 shows global maps of SABER GW momentum

flux for (Figures 9a, 9c, and 9e) January and (Figures 9b, 9d, and 9f) July 2006 at 30 km (Figures 9a and 9b), 50 km (Figures 9c and 9d), and 70 km (Figures 9e and 9f) altitude. The horizontal maps at 30 km altitude (Figures 9a and 9b) are very similar to the HIRDLS global distributions of GW momentum flux for the same months, shown in Figures 3a and 3c. Momentum flux values are enhanced in the polar night jets at mid and high latitudes. In addition, values are enhanced in the subtropics of the summer hemisphere over the monsoon regions, forming a very characteristic zonal triple structure in the northern hemisphere and a triple or quadruple structure in the southern hemisphere.

[149] At 50 km altitude (Figures 9c and 9d) this structure is still well preserved. There is also little change in the relative structure of the high values of GW momentum flux in the southern polar night jet (see Figure 9d). Different from this, momentum flux is strongly reduced in the northern polar night jet (see Figure 9c). In addition, the zonal distribution of momentum flux has changed and has become more patchy. This change and the strong decrease might be related to the stratospheric warming which took place in the northern winter 2005/2006.

[150] At 70 km altitude (Figures 9e and 9f) the momentum flux distribution in both polar night jets has completely changed, compared to 30 km altitude. Momentum flux has strongly decreased and the zonal distribution has become very patchy, indicating that strong GW dissipation has occurred between 50 and 70 km altitude.

[151] In the summer hemisphere the momentum flux distribution still shows the characteristic multiple structure observed at 30 km altitude, but somewhat smeared out. Further, the location of the momentum flux maxima has shifted poleward by about 15° latitude. At 70 km altitude these maxima are now the dominant structures of the global GW momentum flux distribution. The fact that the longitudinal structure of the monsoon regions is still preserved at higher altitudes is further evidence that these maxima are indeed caused by GWs that were originally generated in the monsoon regions at low latitudes and have undergone a latitudinal shift.

7.2. Implications for the Dynamics of the Quasi Two-Day Wave

[152] The non-uniform longitudinal distribution of GW momentum flux (and GW drag) on the summer hemisphere will also have strong influences on the dynamics of the mesosphere. For example, it has been shown by *Holton* [1984] that the longitudinal structure of GW forcing has an impact on the generation of planetary-scale waves in the mesosphere. One of the most prominent global-scale wave modes in the mesosphere is the quasi two-day wave. This wave mode has a period of about two days and a global structure similar to a westward propagating planetary Rossby-gravity normal mode [e.g., *Salby*, 1984] with zonal wavenumber 3 or 4.

[153] Modeling studies indicate that the quasi two-day wave is likely forced in situ and not in the troposphere [e.g., *Jacobi et al.*, 2006a], and it is further indicated that the two-day wave is forced and maintained by breaking GWs [e.g., *Norton and Thuburn*, 1996]. *Limpasuvan and Wu* [2003] investigated quasi two-day wave variations in mesospheric temperature and water vapor derived from UARS MLS observations. The characteristics of these observations also support breaking GWs as a mechanism for the generation of the two-day wave. *Limpasuvan and Wu* [2003] further argued that the longitudinal structure of the GW distribution observed in the stratosphere should have an influence on the global structure of the two-day wave. Observations of GWs in the mesosphere were however missing at that time.

[154] Our study now provides first evidence that, indeed, there is a longitudinal structure in the GW momentum fluxes, likely originating from GWs generated by deep convection in the subtropics of the summer hemisphere. Further, it should be noted that those summertime maxima of GW momentum fluxes start somewhat earlier than the occurrence of the quasi two-day waves. First enhancements of GW momentum fluxes in the mesosphere in these maxima are about 1–2 months before the summer solstices (see Figure 7d), while quasi two-day waves occur around the summer solstices and somewhat later [e.g., *Ern et al.*, 2009a].

[155] These three facts together suggest that, first, the quasi two-day waves are excited by the GWs generated in the subtropical monsoon regions, and, second, that the zonal wavenumbers 3 and 4 that are characteristic for the quasi two-day waves might be caused by the longitudinal variation of the monsoon regions which is still partly preserved in the mesosphere.

[156] Of course, the summer hemisphere momentum flux maxima do not display a plain zonal wavenumber 3 or 4 structure. In Figure 9 there are also indications of zonal wavenumbers 1 and 2. The contributions of the different wavenumbers will additionally vary with altitude, and explanations how this leads to the forcing of a zonal wavenumber 3 or 4 quasi two-day wave will not be simple. In particular, interactions between GWs and tides might play an important role. A more detailed analysis is however beyond the scope of our current study.

8. Summary

[157] Values of gravity wave (GW) squared temperature amplitudes, vertical and horizontal wavelengths, as well as absolute values of GW momentum flux have been derived from HIRDLS and SABER data. For this purpose the global-scale background temperature distribution has been removed by a 2d-Fourier decomposition in longitude and time. This method is also capable to remove global-scale waves with periods as short as about 1–2 days and thus global distributions of GW momentum flux absolute values can be derived not only in the stratosphere, but for the first time also in the mesosphere.

[158] Seasonal variations show enhanced GW momentum fluxes in the polar night jets, as well as over the monsoon regions in the subtropics of the summer hemisphere. There are indications that the GWs generated in the monsoon regions are shifted poleward by about 15° latitude when propagating from 30 to 70 km altitude.

[159] To find out where the most significant interactions between GWs and the background wind can be expected, we have calculated "potential accelerations" due to GWs from absolute values of GW momentum flux. High values of potential accelerations suggest that GWs strongly interact with the polar night jets not only in the mesosphere, but already in the stratosphere. This effect is currently under-

estimated in GCM simulations and could be important for the downward coupling between stratosphere and troposphere and consequently for the predictive skill of GCMs in a changing climate. In addition, GWs generated in the monsoon regions of the summer hemisphere likely make a large contribution to the overall momentum budget where the poleward tilt in the mesospheric summer jets is observed. Therefore it might be important to include the effect of non-vertical propagation of GWs into GCMs in future.

[160] In the middle and upper mesosphere the monsoon related momentum flux maxima are the dominant feature of the global distribution of GW momentum flux. This is the case because of the strong dissipation of the GWs in the polar night jets already in the stratosphere and lower mesosphere. The characteristic longitudinal variation of those monsoon related momentum flux maxima can still be seen in the mesosphere. The resulting longitudinal non-uniformity of GW drag could play an important role in the generation of the quasi two-day wave.

[161] Besides seasonal variations we also find likely QBO-related variations in the amplitudes and momentum fluxes of the GWs generated in the monsoon regions. This effect is particularly strong in the northern hemisphere. In the nine years of SABER data available we find also longer-term variations that might indicate an anti-correlation between solar activity and GW momentum flux. However, also other decadal variations, not directly related to the 11-year solar cycle, could be a possible reason for the observed effect.

[162] **Acknowledgments.** Very helpful comments by three anonymous reviewers are gratefully acknowledged. The work of M. Ern was supported by the Deutsche Forschungsgemeinschaft (DFG) within the project GW-EXCITES (grant ER 474/2–1), which is part of the DFG priority program CAWSES (SPP–1176). This work further largely benefited from the SPARC gravity wave initiative, as well as "The Gravity Wave Project" (ISSI Team 161) led by M.J. Alexander and organized by the International Space Science Institute (ISSI), Bern. The SPARC zonal wind climatology was provided by the SPARC data center. Monthly Singapore winds were obtained from Free University of Berlin and monthly solar flux data from NOAA. SABER data were provided by GATS Inc., and HIRDLS data by NASA. Many thanks also go to the teams of the HIRDLS and SABER instruments for all their effort to create the excellent data sets used in this study.

References

Alexander, M. J., and T. J. Dunkerton (1999), A spectral parameterization of mean-flow forcing due to breaking gravity waves, *J. Atmos. Sci.*, *56*, 4167–4182.

Alexander, M. J., and D. A. Ortland (2010), Equatorial waves in High Resolution Dynamics Limb Sounder (HIRDLS) data, *J. Geophys. Res.*, *115*, D24111, doi:10.1029/2010JD014782.

Alexander, M. J., et al. (2008), Global estimates of gravity wave momentum flux from High Resolution Dynamics Limb Sounder Observations, *J. Geophys. Res.*, *113*, D15S18, doi:10.1029/2007JD008807.

Alexander, M. J., et al. (2010), Recent developments in gravity-wave effects in climate models and the global distribution of gravity-wave momentum flux from observations and models, *Q. J. R. Meteorol. Soc.*, *136*, 1103–1124, doi:10.1002/qj.637.

Baldwin, M. P., and T. J. Dunkerton (1999), Propagation of the Arctic Oscillation from the stratosphere to the troposphere, *J. Geophys. Res.*, *104*, 30,937–30,946.

Baldwin, M. P., and T. J. Dunkerton (2001), Stratospheric harbingers of anomalous weather regimes, *Science*, *294*, 581–584.

Becker, E., and D. C. Fritts (2006), Enhanced gravity-wave activity and interhemispheric coupling during the MaCWAVE/MIDAS northern summer program 2002, *Ann. Geophys.*, *24*, 1175–1188.

Brewer, A. W. (1949), Evidence for a world circulation provided by the measurements of helium and water vapor distribution in the stratosphere, *Q. J. R. Meteorol. Soc.*, *75*, 351–363.

Charron, M., and E. Manzini (2002), Gravity waves from fronts: Parameterization and middle atmosphere response in a general circulation model, *J. Atmos. Sci.*, *59*, 923–941.

de la Torre, A., T. Schmidt, and J. Wickert (2006), A global analysis of wave potential energy in the lower and middle atmosphere from CHAMP and SAC-C GPS-RO long term data, *Geophys. Res. Lett.*, *33*, L24809, doi:10.1029/2006GL027696.

Dobson, G. M. B. (1956), Origin and distribution of the polyatomic molecules in the atmosphere, *Proc. R. Soc. London, Ser. A 236*, 187–193.

Dunkerton, T. J. (1997), The role of gravity waves in the quasi-biennial oscillation, *J. Geophys. Res.*, *102*, 26,053–26,076.

Eckermann, S. D., and P. Preusse (1999), Global measurements of stratospheric mountain waves from space, *Science*, *286*, 1534–1537, doi:10.1126/science.286.5444.1534.

Ern, M., and P. Preusse (2009a), Wave fluxes of equatorial Kelvin waves and QBO zonal wind forcing derived from SABER and ECMWF temperature space-time spectra, *Atmos. Chem. Phys.*, *9*, 3957–3986, doi:10.5194/acp-9-3957-2009.

Ern, M., and P. Preusse (2009b), Quantification of the contribution of equatorial Kelvin waves to the QBO wind reversal in the stratosphere, *Geophys. Res. Lett.*, *36*, L21801, doi:10.1029/2009GL040493.

Ern, M., P. Preusse, M. J. Alexander, and C. D. Warner (2004), Absolute values of gravity wave momentum flux derived from satellite data, *J. Geophys. Res.*, *109*, D20103, doi:10.1029/2004JD004752.

Ern, M., P. Preusse, and C. D. Warner (2005), A comparison between CRISTA satellite data and Warner and McIntyre gravity wave parameterization scheme: Horizontal and vertical wavelength filtering of gravity wave momentum flux, *Adv. Space Res.*, *35*, 2017–2023, doi:10.1016/j.asr.2005.04.109.

Ern, M., P. Preusse, and C. D. Warner (2006), Some experimental constraints for spectral parameters used in the Warner and McIntyre gravity wave parameterization scheme, *Atmos. Chem. Phys.*, *6*, 4361–4381, doi:10.5194/acp-6-4361-2006.

Ern, M., P. Preusse, M. Krebsbach, M. G. Mlynczak, and J. M. Russell III (2008), Equatorial wave analysis from SABER and ECMWF temperatures, *Atmos. Chem. Phys.*, *8*, 845–869, doi:10.5194/acp-8-845-2008.

Ern, M., C. Lehmann, M. Kaufmann, and M. Riese (2009a), Spectral wave analysis at the mesopause from SCIAMACHY airglow data compared to SABER temperature spectra, *Ann. Geophys.*, *27*, 407–416.

Ern, M., H.-K. Cho, P. Preusse, and S. D. Eckermann (2009b), Properties of the average distribution of equatorial Kelvin waves investigated with the GROGRAT ray tracer, *Atmos. Chem. Phys.*, *9*, 7973–7995, doi:10.5194/acp-9-7973-2009.

Fetzer, E. J., and J. C. Gille (1994), Gravity wave variances in LIMS temperatures: I. Variability and comparison with background winds, *J. Atmos. Sci.*, *51*, 2461–2483.

Forbes, J. M., J. Russell, S. Miyahara, X. Zhang, S. Palo, M. Mlynczak, C. J. Mertens, and M. E. Hagan (2006), Troposphere-thermosphere tidal coupling as measured by the SABER instrument on TIMED during July–September 2002, *J. Geophys. Res.*, *111*, A10S06, doi:10.1029/2005JA011492.

Fritts, D. C., and M. J. Alexander (2003), Gravity wave dynamics and effects in the middle atmosphere, *Rev. Geophys.*, *41*(1), 1003, doi:10.1029/2001RG000106.

Fritts, D. C., and T. E. VanZandt (1993), Spectral estimates of gravity wave energy and momentum fluxes. Part I: Energy dissipation, acceleration, and constraints, *J. Atmos. Sci.*, *50*, 3685–3694.

Fröhlich, K., T. Schmidt, M. Ern, P. Preusse, A. de la Torre, J. Wickert, and C. Jacobi (2007), The global distribution of gravity wave energy in the lower stratosphere derived from GPS data and gravity wave modelling: attempt and challenges, *J. Atmos. Sol. Terr. Phys.*, *69*, 2238–2248, doi:10.1016/j.jastp.2007.07.005.

Garcia, R. R., and W. J. Randel (2008), Acceleration of the Brewer Dobson circulation due to increases in greenhouse gases, *J. Atmos. Sci.*, *65*, 2731–2739.

Garcia, R. R., R. Lieberman, J. M. Russell III, and M. G. Mlynczak (2005), Large-scale waves in the mesosphere and lower thermosphere observed by SABER, *J. Atmos. Sci.*, *62*, 4384–4399.

Gardner, C. S. (1994), Diffusive filtering theory of gravity wave spectra in the atmosphere, *J. Geophys. Res.*, *99*, 20,601–20,622.

Gavrilov, N. M., A. H. Manson, and C. E. Meek (1995), Climatological monthly characteristics of middle atmosphere gravity waves (10 min–10 h) during 1979–1993 at Saskatoon, *Ann. Geophys.*, *13*, 285–295.

Gavrilov, N. M., S. Fukao, T. Nakamura, C. Jacobi, D. Kürschner, A. H. Manson, and C. E. Meek (2002), Comparative study of interannual changes of the mean winds and gravity wave activity in the middle atmo-

sphere over Japan, Central Europe and Canada, *J. Atmos. Sol. Terr. Phys.*, *64*, 1003–1010.

Gavrilov, N. M., D. M. Riggin, and D. C. Fritts (2004), Interannual variations of the mean wind and gravity wave variances in the middle atmosphere over Hawaii, *J. Atmos. Sol. Terr. Phys.*, *66*, 637–645, doi:10.1016/j.jastp.2004.01.015.

Gille, J. C., J. J. Barnett, J. Whitney, M. Dials, D. Woodard, W. Rudolf, A. Lambert, and W. Mankin (2003), The High Resolution Dynamics Limb Sounder (HIRDLS) experiment on Aura, *Proc. SPIE Int. Soc. Opt. Eng.*, *5152*, 162–171.

Gille, J. C., et al. (2008), High Resolution Dynamics Limb Sounder: Experiment overview, recovery, and validation of initial temperature data, *J. Geophys. Res.*, *113*, D16S43, doi:10.1029/2007JD008824.

Giorgetta, M. A., L. Bengtsson, and K. Arpe (1999), An investigation of QBO signals in the east Asian and Indian monsoon in GCM experiments, *Clim. Dyn.*, *15*, 435–450.

Gong, J., M. A. Geller, and L. Wang (2008), Source spectra information derived from U.S. high-resolution radiosonde data, *J. Geophys. Res.*, *113*, D10106, doi:10.1029/2007JD009252.

Grossmann, K. U., D. Offermann, O. Gusev, J. Oberheide, M. Riese, and R. Spang (2002), The CRISTA-2 Mission, *J. Geophys. Res.*, *107*(D23), 8173, doi:10.1029/2001JD000667.

Hertzog, A., G. Boccara, R. A. Vincent, F. Vial, and P. Coquerez (2008), Estimation of gravity-wave momentum flux and phase speeds from long-duration stratospheric balloon flights: 2. Results from the Vorcore campaign in Antarctica, *J. Atmos. Sci.*, *65*, 3056–3070.

Hines, C. O. (1997a), Doppler-spread parameterization of gravity-wave momentum deposition in the middle atmosphere. Part 1: Basic formulation, *J. Atmos. Sol. Terr. Phys.*, *59*, 371–386.

Hines, C. O. (1997b), Doppler-spread parameterization of gravity-wave momentum deposition in the middle atmosphere. Part 2: Broad and quasi monochromatic spectra and implementation, *J. Atmos. Sol. Terr. Phys.*, *59*, 387–400.

Hoffmann, L., and M. J. Alexander (2010), Occurrence frequency of convective gravity waves during the North American thunderstorm season, *J. Geophys. Res.*, *115*, D20111, doi:10.1029/2010JD014401.

Hoffmann, P., W. Singer, D. Keuer, W. K. Hocking, M. Kunze, and Y. Murayama (2007), Latitudinal and longitudinal variability of mesospheric winds and temperatures during stratospheric warming events, *J. Atmos. Sol. Terr. Phys.*, *69*, 2355–2366, doi:10.1016/j.jastp.2007.06.010.

Holton, J. R. (1982), The role of gravity wave induced drag and diffusion in the momentum budget of the mesosphere, *J. Atmos. Sci.*, *39*, 791–799.

Holton, J. R. (1983), The influence of gravity wave breaking on the general circulation of the middle atmosphere, *J. Atmos. Sci.*, *40*, 2497–2507.

Holton, J. R. (1984), The generation of mesospheric planetary waves by zonally asymmetric gravity wave breaking, *J. Atmos. Sci.*, *41*, 3427–3430.

Holton, J. R., and H.-C. Tan (1980), The influence of the equatorial quasi-biennial oscillation on the global circulation at 50 mb, *J. Atmos. Sci.*, *37*, 2200–2208.

Jacobi, C., K. Fröhlich, and A. Pogoreltsev (2006a), Quasi two-day-wave modulation of gravity wave flux and consequences for the planetary wave propagation in a simple circulation model, *J. Atmos. Sol. Terr. Phys.*, *68*, 283–292, doi:10.1016/j.jastp.2005.01.017.

Jacobi, C., N. M. Gavrilov, D. Kürschner, and K. Fröhlich (2006b), Gravity wave climatology and trends in the mesosphere/lower thermosphere region deduced from low-frequency drift measurements 1984–2003 (52.1°N, 13.2°E), *J. Atmos. Sol. Terr. Phys.*, *68*, 1913–1923, doi:10.1016/j.jastp.2005.12.007.

Jiang, J. H., S. D. Eckermann, D. L. Wu, and J. Ma (2004a), A search for mountain waves in MLS stratospheric limb radiances from the winter Northern Hemisphere: Data analysis and global mountain wave modeling, *J. Geophys. Res.*, *109*, D03107, doi:10.1029/2003JD003974.

Jiang, J. H., B. Wang, K. Goya, K. Hocke, S. D. Eckermann, J. Ma, D. L. Wu, and W. G. Read (2004b), Geographical distribution and interseasonal variability of tropical deep convection: UARS MLS observations and analyses, *J. Geophys. Res.*, *109*, D03111, doi:10.1029/2003JD003756.

Karlsson, B., C. E. Randall, S. Benze, M. Mills, V. L. Harvey, S. M. Bailey, and J. M. Russell III (2009), Intra-seasonal variability of polar mesospheric clouds due to inter-hemispheric coupling, *Geophys. Res. Lett.*, *36*, L20802, doi:10.1029/2009GL040348.

Kawatani, Y., K. Sato, T. J. Dunkerton, S. Watanabe, S. Miyahara, and M. Takahashi (2010a), The roles of equatorial trapped waves and internal inertia gravity waves in driving the quasi-biennial oscillation. Part I: Zonal mean wave forcing, *J. Atmos. Sci.*, *67*, 963–980, doi:10.1175/2009JAS3222.1.

Kawatani, Y., K. Sato, T. J. Dunkerton, S. Watanabe, S. Miyahara, and M. Takahashi (2010b), The roles of equatorial trapped waves and internal inertia gravity waves in driving the quasi-biennial oscillation. Part II: Three-dimensional distribution of wave forcing, *J. Atmos. Sci.*, *67*, 981–997, doi:10.1175/2009JAS3223.1.

Kim, Y.-J., S. D. Eckermann, and H.-Y. Chun (2003), An overview of the past, present and future of gravity-wave drag parametrization for numerical climate and weather prediction models, *Atmos. Ocean*, *41*, 65–98.

Krebsbach, M., and P. Preusse (2007), Spectral analysis of gravity wave activity in SABER temperature data, *Geophys. Res. Lett.*, *34*, L03814, doi:10.1029/2006GL028040.

Lait, L. R., and J. L. Stanford (1988a), Applications of asynoptic space-time Fourier transform methods to scanning satellite measurements, *J. Atmos. Sci.*, *45*, 3784–3799.

Lait, L. R., and J. L. Stanford (1988b), Fast, long-lived features in the polar stratosphere, *J. Atmos. Sci.*, *45*, 3800–3809.

Li, F., J. Austin, and J. Wilson (2008), The strength of the Brewer Dobson circulation in a changing climate: Coupled chemistry climate model simulations, *J. Clim.*, *21*, 40–57, doi:10.1175/2007JCLI1663.1.

Limpasuvan, V., and D. L. Wu (2003), Two-day wave observations of UARS Microwave Limb Sounder mesospheric water vapor and temperature, *J. Geophys. Res.*, *108*(D10), 4307, doi:10.1029/2002JD002903.

Lindzen, R. S. (1981), Turbulence and stress due to gravity wave and tidal breakdown, *J. Geophys. Res.*, *86*, 9707–9714.

Manney, G. L., et al. (2008), The evolution of the stratopause during the 2006 major warming: Satellite data and assimilated meteorological analyses, *J. Geophys. Res.*, *113*, D11115, doi:10.1029/2007JD009097.

Manzini, E., and N. A. McFarlane (1998), The effect of varying the source spectrum of a gravity wave parameterization in a middle atmosphere general circulation model, *J. Geophys. Res.*, *103*(D24), 31,523–31,539.

Marshall, A. G., and A. A. Scaife (2009), Impact of the QBO on surface winter climate, *J. Geophys. Res.*, *114*, D18110, doi:10.1029/2009JD011737.

McLandress, C., and T. G. Shepherd (2009), Simulated anthropogenic changes in the Brewer Dobson circulation, including its extension to high latitudes, *J. Clim.*, *22*, 1516–1540, doi:10.1175/2008JCLI2679.1.

Mieth, P., J. L. Grenfell, U. Langematz, and M. Kunze (2004), Sensitivity of the Freie Universität Berlin Climate Middle Atmosphere Model (FUB–CMAM) to different gravity-wave drag parameterisations, *Ann. Geophys.*, *22*, 2693–2713.

Mlynczak, M. G. (1997), Energetics of the mesosphere and lower thermosphere and the SABER instrument, *Adv. Space Res.*, *44*, 1177–1183.

Mohankumar, K., and P. A. Pillai (2008), Stratosphere troposphere interaction associated with biennial oscillation of Indian summer monsoon, *J. Atmos. Sol. Terr. Phys.*, *70*, 764–773, doi:10.1016/j.jastp.2007.12.001.

Monier, E., and B. C. Weare (2011), Climatology and trends in the forcing of the stratospheric mean flow, *Atmos. Chem. Phys. Discuss.*, *11*, 11,649–11,690, doi:10.5194/acpd-11-11649-2011.

Mukhtarov, P., D. Pancheva, and B. Andonov (2009), Global structure and seasonal and interannual variability of the migrating diurnal tide seen in the SABER/TIMED temperatures between 20 and 120 km, *J. Geophys. Res.*, *114*, A02309, doi:10.1029/2008JA013759.

Norton, W. A., and J. Thuburn (1996), The two-day wave in a middle atmosphere GCM, *Geophys. Res. Lett.*, *23*, 2113–2116.

Offermann, D., K. U. Grossmann, P. Barthol, P. Knieling, M. Riese, and R. Trant (1999), The cryogenic infrared spectrometers and telescopes for the atmosphere (CRISTA) experiment and middle atmosphere variability, *J. Geophys. Res.*, *104*, 16,311–16,325.

Orr, A., P. Bechtold, J. F. Scinocca, M. Ern, and M. Janiskova (2010), Improved middle atmosphere climate and forecasts in the ECMWF model through a nonorographic gravity wave drag parameterization, *J. Clim.*, *23*, 5905–5926, doi:10.1175/2010JCLI3490.1.

Pancheva, D., P. Mukhtarov, and B. Andonov (2010), Global structure, seasonal and interannual variability of the eastward propagating tides seen in the SABER/TIMED temperatures (2002–2007), *Adv. Space Res.*, *46*, 257–274, doi:10.1016/j.asr.2010.03.026.

Preusse, P., A. Dörnbrack, S. D. Eckermann, M. Riese, B. Schaeler, J. T. Bacmeister, D. Broutman, and K. U. Grossmann (2002), Space-based measurements of stratospheric mountain waves by CRISTA, 1. Sensitivity, analysis method, and a case study, *J. Geophys. Res.*, *107*(D23), 8178, doi:10.1029/2001JD000699.

Preusse, P., S. D. Eckermann, M. Ern, F. J. Schmidlin, M. J. Alexander, and D. Offermann (2003), Infrared limb sounding measurements of middle atmosphere gravity waves by CRISTA, *Proc. SPIE Int. Soc. Opt. Eng.*, *4882*, 134–148.

Preusse, P., et al. (2006), Tropopause to mesopause gravity waves in August: Measurement and modeling, *J. Atmos. Sol. Terr. Phys.*, *68*, 1730–1751, doi:10.1016/j.jastp.2005.10.019.

Preusse, P., S. D. Eckermann, and M. Ern (2008), Transparency of the atmosphere to short horizontal wavelength gravity waves, *J. Geophys. Res.*, *113*, D24104, doi:10.1029/2007JD009682.

Preusse, P., S. Schroeder, L. Hoffmann, M. Ern, F. Friedl-Vallon, H. Oelhaf, H. Fischer, and M. Riese (2009a), New perspectives on gravity wave remote sensing by spaceborne infrared limb imaging, *Atmos. Meas. Tech.*, *2*, 299–311.

Preusse, P., S. D. Eckermann, M. Ern, J. Oberheide, R. H. Picard, R. G. Roble, M. Riese, J. M. Russell III, and M. G. Mlynczak (2009b), Global ray tracing simulations of the SABER gravity wave climatology, *J. Geophys. Res.*, *114*, D08126, doi:10.1029/2008JD011214.

Randel, W., M.-L. Chanin, and C. Michaut (2002), SPARC intercomparison of middle atmosphere climatologies, *WMO/TD–No. 1142*, World Meteorol. Org., Geneva, Switzerland.

Randel, W., et al. (2004), The SPARC intercomparison of middle atmosphere climatologies, *J. Clim.*, *17*, 986–1003.

Ray, E. A., M. J. Alexander, and J. R. Holton (1998), An analysis of the structure and forcing of the equatorial semiannual oscillation in zonal wind, *J. Geophys. Res.*, *103*, 1759–1774.

Remsberg, E. E., L. L. Gordley, B. T. Marshall, R. E. Thompson, J. Burton, P. Bhatt, V. L. Harvey, G. Lingenfelser, and M. Natarajan (2004), The Nimbus 7 LIMS version 6 radiance conditioning and temperature retrieval methods and results, *J. Quant. Spectrosc. Radiat. Transfer*, *86*, 395–424, doi:10.1016/j.jqsrt.2003.12.007.

Remsberg, E. E., et al. (2008), Assessment of the quality of the Version 1.07 temperature-versus-pressure profiles of the middle atmosphere from TIMED/SABER, *J. Geophys. Res.*, *113*, D17101, doi:10.1029/2008JD010013.

Richter, J. H., F. Sassi, and R. R. Garcia (2010), Toward a physically based gravity wave source parameterization in a general circulation model, *J. Atmos. Sci.*, *67*, 136–156, doi:10.1175/2009JAS3112.1.

Riese, M., P. Preusse, R. Spang, M. Ern, M. Jarisch, K. U. Grossmann, and D. Offermann (1997), Measurements of trace gases by the cryogenic infrared spectrometers and telescopes for the atmosphere (CRISTA) experiment, *Adv. Space Res.*, *19*, 563–566.

Riese, M., R. Spang, P. Preusse, M. Ern, M. Jarisch, D. Offermann, and K. U. Grossmann (1999), Cryogenic infrared spectrometers and telescopes for the atmosphere (CRISTA) data processing and atmospheric temperature and trace gas retrieval, *J. Geophys. Res.*, *104*, 16,349–16,367.

Russell, J. M., III, M. G. Mlynczak, L. L. Gordley, J. Tansock, and R. Esplin (1999), An overview of the SABER experiment and preliminary calibration results, *Proc. SPIE Int. Soc. Opt. Eng.*, *3756*, 277–288.

Salby, M. L. (1982a), Sampling theory for asynoptic satellite observations, Part I: Space-time spectra, resolution, and aliasing, *J. Atmos. Sci.*, *39*, 2577–2600.

Salby, M. L. (1982b), Sampling theory for asynoptic satellite observations, Part II: Fast Fourier synoptic mapping, *J. Atmos. Sci.*, *39*, 2601–2614.

Salby, M. L. (1984), Survey of planetary-scale traveling waves: The state of theory and observations, *Rev. Geophys.*, *22*, 209–236.

Sato, K., S. Watanabe, Y. Kawatani, Y. Tomikawa, K. Miyazaki, and M. Takahashi (2009), On the origins of mesospheric gravity waves, *Geophys. Res. Lett.*, *36*, L19801, doi:10.1029/2009GL039908.

Scinocca, J. F. (2003), An accurate spectral nonorographic gravity wave drag parameterization for general circulation models, *J. Atmos. Sci.*, *60*, 667–682.

Sigmond, M., J. F. Scinocca, and P. J. Kushner (2008), Impact of the stratosphere on tropospheric climate change, *Geophys. Res. Lett.*, *35*, L12706, doi:10.1029/2008GL033573.

Song, I.-S., and H.-Y. Chun (2008), A Lagrangian spectral parameterization of gravity wave drag induced by Cumulus convection, *J. Atmos. Sci.*, *65*, 1204–1224.

Swinbank, R., and D. A. Ortland (2003), Compilation of wind data for the Upper Atmosphere Research Satellite (UARS) Reference Atmosphere Project, *J. Geophys. Res.*, *108*(D19), 4615, doi:10.1029/2002JD003135.

Tsuda, T., M. Nishida, C. Rocken, and R. H. Ware (2000), A global morphology of gravity wave activity in the stratosphere revealed by the GPS occultation data (GPS/MET), *J. Geophys. Res.*, *105*, 7257–7273.

Ungermann, J., L. Hoffmann, P. Preusse, M. Kaufmann, and M. Riese (2010), Tomographic retrieval approach for mesoscale gravity wave observations by the PREMIER Infrared Limb-Sounder, *Atmos. Meas. Tech.*, *3*, 339–354.

Wang, L., and M. J. Alexander (2009), Gravity wave activity during stratospheric sudden warmings in the 2007–2008 Northern Hemisphere winter, *J. Geophys. Res.*, *114*, D18108, doi:10.1029/2009JD011867.

Wang, L., and M. J. Alexander (2010), Global estimates of gravity wave parameters from GPS radio occultation temperature data, *J. Geophys. Res.*, *115*, D21122, doi:10.1029/2010JD013860.

Warner, C. D., and M. E. McIntyre (1996), On the propagation and dissipation of gravity wave spectra through a realistic middle atmosphere, *J. Atmos. Sci.*, *53*, 3213–3235.

Warner, C. D., and M. E. McIntyre (2001), An ultrasimple spectral parameterization for nonorographic gravity waves, *J. Atmos. Sci.*, *58*, 1837–1857.

Warner, C. D., A. A. Scaife, and N. Butchart (2005), Filtering of parameterized nonorographic gravity waves in the Met Office unified model, *J. Atmos. Sci.*, *62*, 1831–1848.

Watanabe, S., Y. Kawatani, Y. Tomikawa, K. Miyazaki, M. Takahashi, and K. Sato (2008), General aspects of a T213L256 middle atmosphere general circulation model, *J. Geophys. Res.*, *113*, D12110, doi:10.1029/2008JD010026.

Wright, C. J., S. M. Osprey, J. J. Barnett, L. J. Gray, and J. C. Gille (2010), High Resolution Dynamics Limb Sounder measurements of gravity wave activity in the 2006 Arctic stratosphere, *J. Geophys. Res.*, *115*, D02105, doi:10.1029/2009JD011858.

Wu, D. L., E. F. Fishbein, W. G. Read, and J. W. Waters (1996), Excitation and evolution of the quasi-2-day wave observed in UARS/MLS temperature measurements, *J. Atmos. Sci.*, *53*, 728–738.

Yan, X., N. Arnold, and J. J. Remedios (2010), Global observations of gravity waves from High Resolution Dynamics Limb Sounder temperature measurements: A yearlong record of temperature amplitude and vertical wavelength, *J. Geophys. Res.*, *115*, D10113, doi:10.1029/2008JD011511.

M. Ern, P. Preusse, and M. Riese, Institut für Energie- und Klimaforschung – Stratosphäre, Forschungszentrum Jülich, D-52425 Jülich, Germany. (m.ern@fz-juelich.de)

J. C. Gille, Center for Limb Atmospheric Sounding, University of Colorado at Boulder, Boulder, CO 80309-0440, USA.

C. L. Hepplewhite, Atmospheric, Oceanic, and Planetary Physics, Department of Physics, University of Oxford, Parks Road, Oxford OX1 3PU, UK.

M. G. Mlynczak, NASA Langley Research Center, Hampton, VA 23681-0001, USA.

J. M. Russell III, Center for Atmospheric Sciences, Hampton University, Hampton, VA 23668, USA.